






# Defect-mediated dynamics of coherent structures in active nematics

Received: 3 April 2021

Accepted: 20 April 2023

Published online: 25 May 2023

 Check for updates

Mattia Serra <sup>1,2</sup> , Linnea Lemma<sup>3</sup>, Luca Giomi <sup>4</sup>, Zvonimir Dogic<sup>3</sup> & L. Mahadevan <sup>2,5,6</sup> 


Active fluids, such as cytoskeletal filaments, bacterial colonies and epithelial cell layers, exhibit distinctive orientational coherence, often characterized by nematic order and its breakdown, defined by the presence of topological defects. In contrast, little is known about positional coherence, that is, whether there is an organization in the underlying fluid motion—despite this being both a prominent and an experimentally accessible feature. Here we characterize the organization of fluid motion in active nematics using the notion of Lagrangian coherent structures by analyzing experimental data of two-dimensional mixtures of microtubules and kinesin, as well as numerical data obtained from the simulation of the active nematodynamic equations. Coherent structures consist of moving attractors and repellers, which orchestrate complex motion. To understand the interaction of positional and orientational coherence, we analyse experiments and simulations and find that  $+1/2$  defects move and deform the attractors, functioning as control centres for collective motion. Additionally, we find that regions around isolated  $+1/2$  defects undergo high bending and low stretching/shearing deformations, consistent with the local stress distribution. The stress is the minimum at the defect, whereas high differential stress along the defect orientation induces folding. Our work offers a new perspective to describe and control self-organization in active fluids, with potential applications to multicellular systems.

Many out-of-equilibrium systems, from bird flocks down to biofilms and the cell cytoskeleton, consist of agents that consume energy and self-organize into large-scale patterns and collectively moving structures<sup>1–9</sup>, which are breathtaking in their beauty and complexity and relevant for embryonic development, wound healing and cancer<sup>10–13</sup>. Understanding the mechanisms that lead to these patterns and characterizing the phases of active matter systems will unravel their complexity, suggesting ways to mimic them using synthetic materials and eventually control and design active systems using external fields.

Self-organized patterns are typically described in Eulerian coordinates, where the local velocity, pressure and orientation of the active building blocks are treated as fields within a fixed laboratory

frame. Two-point correlation functions, spectral densities and other quantities inspired by studies of statistical steady states of turbulence in Newtonian fluids, are typical outcomes of this approach<sup>14,15</sup>. Topological defects, that is, localized singularities in the orientation of the active building blocks<sup>2</sup>, have also been extensively studied and their dynamics are known to be inherently entangled with large-scale chaotic flows<sup>15–17</sup>. But what is the relation between the dynamics of defects and the large-scale coherent motion in flow fields that are typically spatially heterogeneous and temporally unsteady?

A natural framework to address this question is provided by the Lagrangian description of fluid flow. By tracing the motion of passive particles in unsteady flows, which may also include chaotic paths,

<sup>1</sup>Department of Physics, University of California San Diego, San Diego, CA, USA. <sup>2</sup>Paulson School of Engineering and Applied Sciences, Harvard University, Cambridge, MA, USA. <sup>3</sup>Department of Physics, University of California, Santa Barbara, Santa Barbara, CA, USA. <sup>4</sup>Instituut-Lorentz, Universiteit Leiden, Leiden, Netherlands. <sup>5</sup>Department of Organismic and Evolutionary Biology, Harvard University, Cambridge, MA, USA. <sup>6</sup>Department of Physics, Harvard University, Cambridge, MA, USA.  e-mail: [serram@ucsd.edu](mailto:serram@ucsd.edu); [lmahadev@g.harvard.edu](mailto:lmahadev@g.harvard.edu)

one can often identify robust skeletons, commonly referred to as coherent structures (CSs)<sup>18–20</sup>, which shape the trajectory patterns and reveal the organizing barriers to material transport<sup>21,22</sup>. Because we expect our results to hold regardless of the specific Lagrangian integration time, we will often use CSs, which include Lagrangian CSs<sup>18</sup> and their recently developed short-time limits<sup>19,23</sup>. Here we combine theoretical concepts from nonlinear dynamics, active nematodynamics simulations and experiments on suspensions of microtubules and kinesin to unravel the CSs underlying the chaotic flow of two-dimensional active nematics and their relation to the dynamics of topological defects.

## Results

### Lagrangian deformations and CSs

Our theoretical and computational framework for kinematic analysis starts by considering the velocity field  $\mathbf{v}(\mathbf{x}, t)$  of a planar active nematic fluid, and the corresponding flow map

$$\mathbf{F}_{t_0}^t(\mathbf{x}_0) = \mathbf{x}_0 + \int_{t_0}^t \mathbf{v}(\mathbf{F}_{t_0}^\tau(\mathbf{x}_0), \tau) d\tau. \quad (1)$$

This evolves the initial position  $\mathbf{x}_0$  of a virtual tracer particle to the corresponding position  $\mathbf{F}_{t_0}^t(\mathbf{x}_0)$  at time  $t$ , and its spatial derivatives describe the Lagrangian deformation of the nematic fluid over the time interval  $[t_0, t]$ . Locally, a small fluid patch can be stretched, sheared and folded. Stretching and shearing (Fig. 1) are completely characterized by the right Cauchy–Green strain tensor field  $\mathbf{C}_{t_0}^t(\mathbf{x}_0)$  (ref. 24) defined as

$$\mathbf{C}_{t_0}^t(\mathbf{x}_0) = \nabla \mathbf{F}_{t_0}^t(\mathbf{x}_0)^\top \nabla \mathbf{F}_{t_0}^t(\mathbf{x}_0), \quad (2)$$

where  $\nabla \mathbf{F}_{t_0}^t(\mathbf{x}_0)$  is the Jacobian of the flow map.

Given a material patch consisting of straight fibres at initial time (Fig. 1), we use the notation  $\lambda_1 \leq \lambda_2$  and  $\{\boldsymbol{\xi}_1, \boldsymbol{\xi}_2\}$  to denote the eigenvalues and the associated orthonormal eigenvectors of  $\mathbf{C}_{t_0}^t(\mathbf{x}_0)$ . Then one can interpret  $\boldsymbol{\xi}_2$  as the most stretched fibre (by a factor  $\sqrt{\lambda_2}$ ) and  $\boldsymbol{\xi}_1$  is the least stretched one (by a factor  $\sqrt{\lambda_1}$ ). In chaotic systems,  $\lambda_2$  usually grows exponentially in time, it is typically rescaled to read

$$A_{t_0}^t(\mathbf{x}_0) = \frac{1}{|t - t_0|} \log \sqrt{\lambda_2(\mathbf{x}_0)}, \quad (3)$$

which denotes the largest finite-time Lyapunov exponent (FTLE). The maximum stretching along  $\boldsymbol{\xi}_2$  implies that over long times, other fibres align with the local  $\boldsymbol{\xi}_2$  direction (Fig. 1), and follows from an asymptotic analysis of the underlying dynamical system<sup>25</sup>.

By contrast, folding deformations determine variations in the curvature of material fibres over time<sup>26</sup>. This effect can be computed from the second-order spatial derivatives of  $\mathbf{F}_{t_0}^t(\mathbf{x}_0)$  and provides additional information that complements notions of stretching and shearing characterized by first-order spatial derivatives. Starting with an infinitesimal patch of straight fibres at  $\mathbf{x}_0$ , from the  $\boldsymbol{\xi}_2$ -alignment property it follows that the most likely observable fluid folding, during the time interval  $[t_0, t]$ , is the one along the  $\boldsymbol{\xi}_2$  fiber (Fig. 1). This leads to a Lagrangian measure of folding relative to the initial fluid configuration, given by

$$\kappa_{t_0}^t(\mathbf{x}_0, \boldsymbol{\xi}_2) = \frac{[(\nabla^2 \mathbf{F}_{t_0}^t(\mathbf{x}_0) \boldsymbol{\xi}_2) \boldsymbol{\xi}_2] \cdot [\mathbf{R} \nabla \mathbf{F}_{t_0}^t(\mathbf{x}_0) \boldsymbol{\xi}_2]}{\lambda_2^{3/2}}, \quad (4)$$

where  $(\nabla^2 \mathbf{F}_{t_0}^t(\mathbf{x}_0) \boldsymbol{\xi}_2)_{ij} = \sum_k F_{t_0,ijk}^t(\mathbf{x}_0) \boldsymbol{\xi}_{2k}$ ,  $i, j, k \in \{1, 2\}$  and  $\mathbf{R}$  denotes a counterclockwise 90°-rotation matrix (Supplementary Section 1). Analogously, the same folding can be represented at the final

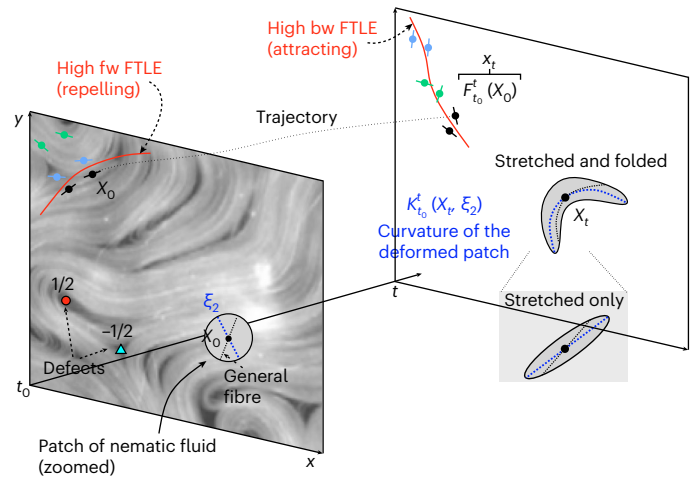


**Fig. 1 | Lagrangian view of an active nematic fluid.** The red curves demarcate the repelling and attracting regions in the flow identified by large values of the forward and backward FTLE. The repellers are based on the initial fluid configuration, whereas the attractors are based on the final configuration. Initially close tracers that are on opposite sides of a forward FTLE ( $\mathcal{A}$ ) ridge will move far apart at time  $t$ . Similarly, initially distant tracers are attracted to a backward FTLE ( $\mathcal{A}$ ) ridge at time  $t$ . Moreover an infinitesimal patch of nematic fluid at  $\mathbf{x}_0$  will get stretched and folded over the time interval  $[t_0, t]$ . Different fibres in this patch tend to align along the fiber  $\boldsymbol{\xi}_2(\mathbf{x}_0)$  corresponding to the maximally stretched direction, and the curvature of the folded patch is  $\kappa_{t_0}^t(\mathbf{x}_t, \boldsymbol{\xi}_2)$ .

position  $\mathbf{x}_t$  by transporting the curvature along the flow trajectories (Fig. 1), so that

$$\kappa_{t_0}^t(\mathbf{x}_t, \boldsymbol{\xi}_2) = \kappa_{t_0}^t(\mathbf{F}_{t_0}^t(\mathbf{x}_0), \boldsymbol{\xi}_2). \quad (5)$$

Large values of  $\kappa_{t_0}^t(\mathbf{x}_0, \boldsymbol{\xi}_2)$  mark the initial positions  $\mathbf{x}_0$  of the nematic fluid that will undergo large folding in the time interval  $[t_0, t]$ , and similarly,  $\kappa_{t_0}^t(\mathbf{x}_t, \boldsymbol{\xi}_2)$  identifies the final positions of the nematic fluid that experience small/large curvature changes (in the Supplementary Section 1, we provide general expressions for the material curvature and its alternative formulation in terms of Eulerian quantities such as flow vorticity, divergence and rate-of-strain tensor). Altogether, equations (3)–(5) completely quantify the maximum stretching and folding deformations of a continuum moving under a given flow map  $\mathbf{F}_{t_0}^t$ . These kinematic measures are model independent and agnostic to the mechanisms driving the flow; hence they are applicable to experimental and computational velocity fields of arbitrary origin and are readily implementable.

In terms of these measures, we can interpret the forward FTLE (fw FTLE or  $\mathcal{A}$ ) as a scalar field over the initial particle positions  $\mathbf{x}_0$  that quantifies the maximum local deformation and identifies the location of maximum spatial separation of initially close particles over the time interval  $[t_0, t]$ . Similarly, the backward FTLE (bw FTLE or  $\mathcal{A}$ ), defined over the final positions  $\mathbf{x}_t$ , identifies the location of the maximum spatial convergence of initially distant particles over  $[t_0, t]$ . Together, they demarcate regions of attraction (attracting CS) and repulsion (repelling CS) (Fig. 1). Despite the fact that FTLE ridges are rarely not material<sup>18</sup>, here we adopt FTLE-based CSs, instead of geodesic ones<sup>18,19</sup>, because we are interested in attraction and repulsion due to both shear and normal deformations, and FTLE CSs are simpler than geodesic CSs to compute and analyse.

### CSs organize particle motion

We now employ these analytical tools to analyse experimental observations of two-dimensional microtubule-based active nematic liquid crystals assembled on a surfactant-stabilized oil–water interface<sup>27</sup>.

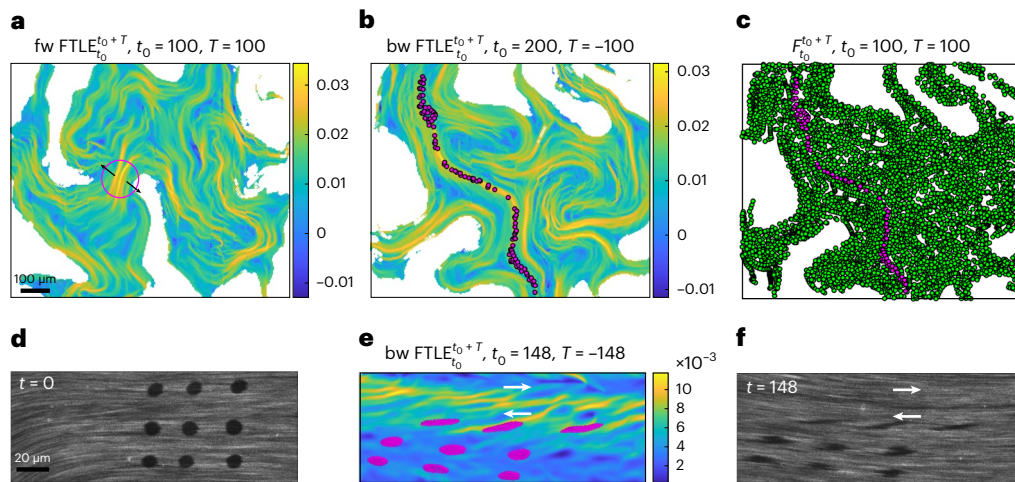


**Fig. 2 | Dynamics of a two-dimensional microtubule-based extensile active nematic system assembled on an oil–water interface.** The PIV based velocity is reconstructed on a uniform  $670 \times 800 \mu\text{m}^2$  grid with a spatial resolution of  $15.6 \mu\text{m}$  and temporal resolution of 1 frame per second. **a**,  $\rho A$  field whose ridges mark repelling CSs. The white regions demarcate the set of particles that left the domain where the velocity field is available. **b**,  $\rho A$  field whose ridges mark attracting CSs. The magenta dots represent the final ( $t = 200$ ) position of the tracers that started inside the magenta circle (shown in **a**) at the initial time  $t = 100$ . **c**, Final position of the tracers that started from a uniform grid at the

initial time. The particles that started outside the magenta circle are indicated in green; see Supplementary Video 1. **d–f**, Fluorescence recovery after photobleaching experiment in active nematics. Initial and final configuration of the fluorescence recovery after photobleaching experiment (**d** and **f**). **e**, The FTLE  $\rho A_{148}^0$  along with advected particles at  $t = 148$ , initialized to correspond to the photobleached regions at  $t = 0$ . Supplementary Video 2 shows the data in **d** and **e** for increasing  $t$ . Time is indicated in seconds (s). The colour bars encode the attraction or repulsion rates (in  $\text{s}^{-1}$ ). In **a–c**, the ATP concentration is  $250 \mu\text{M}$ . In **d–f**, the ATP concentration is  $18 \mu\text{M}$ .

The large-scale chaotic dynamics of these materials is collectively driven by kinesin molecular motors that move along multiple filaments to induce relative filament sliding.

Using particle image velocimetry (PIV), we reconstruct the velocity field of autonomously flowing active nematics. Supplementary Section 2 and Supplementary Figs. 1 and 2 provide details of the PIV-derived velocity and its validation for computing the Lagrangian trajectories. From the velocity field, we compute  $\rho A$  and  $\rho A$  for different timescales  $|T| = |t - t_0|$  using equations (1)–(3). Figure 2a,b shows the  $\rho A$  and  $\rho A$  fields for  $|T| = 100$  s. As sketched in Fig. 1, particles are repelled from a  $\rho A$  ridge and attracted towards a  $\rho A$  ridge (covered by magenta dots). Figure 2c shows the final position of a set of particles initially released from a uniform grid and serves as a tracker of particle motion. Supplementary Video 1 shows the time evolution of the FTLE fields and particle positions. Although the active fluid seems to move chaotically, there is an underlying coherent skeleton, captured by the FTLE fields, that dynamically organizes their motion but remains inaccessible from the mere inspection of fluid tracers.

The FTLE also provides a  $|T|$ -dependent map of the stretching and shearing Lagrangian deformation of the active continuum, with ridges that demarcate sets of the fluid that will experience higher deformations relative to their neighbours. Along the trajectories, the Lagrangian deformation consistently integrates the separate contributions of viscous, elastic and active stresses deforming the nematic fluid and thus encodes a memory trace of the nematodynamic field.

To correlate these computed Lagrangian memory traces with direct observations of the deformation patterns near  $\rho A$  ridges, we label the regions of microtubule-based active nematics and observe their subsequent evolution (Supplementary Section 2). This is achieved by photobleaching nine circular regions with a radius of  $\sim 4 \mu\text{m}$  (Fig. 2d). Using the PIV data, we compute the  $\rho A$  field along with the position of Lagrangian tracers (magenta) initialized at  $t = 0$  in correspondence with the photobleached regions (Fig. 2e). Stripe-shaped ridges of  $\rho A_{148}^0$  reveal a horizontal shear layer, along with regions of distinctly high attraction and Lagrangian deformations. Our analysis predicts the

evolution of advected and diffused photobleached patches (Fig. 2f and Supplementary Video 2). Overall,  $\rho A_{148}^0$  provides a  $|T|$ -dependent map of attraction as well as stretching and shearing deformations maps over the entire domain.

### Positive defects mediate attracting CSs

Having uncovered the organizers of the flow fields using Lagrangian CSs, we now turn to understand if and how they are related to the visible dynamics of topological defects, well known to be correlated with complex, large-scale nematodynamic flows<sup>15,17</sup>. To enable this, we redid our experiments with the microtubule–kinesin system, slowed the dynamics by reducing ATP concentration to  $2 \mu\text{M}$  and simultaneously measured both velocity  $\mathbf{v}$  and nematic director  $\mathbf{n}$  fields (Supplementary Section 2).

We mark  $+1/2$  defects with red dots and  $-1/2$  defects with cyan triangles (Fig. 1). Figure 3a–c shows  $\rho A$  for increasing time intervals, along with the positions of tracers (magenta), initially released from a circular blob and eventually attracted to a  $\rho A$  ridge. Supplementary Video 3 shows the time evolution of  $\rho A$  and  $\rho A$  along with particle positions. The FTLE fields again uncover the organizers of fluid motion that are inaccessible to trajectory plots alone.

Along with  $\rho A$ , Fig. 3a–c shows the evolution of topological defects, with the red arrows indicating the direction of motion of positive defects. These data suggest that positive defects move and deform  $\rho A$  ridges, which, in turn, directs particle motion. Displaying the director field with the  $\rho A$  field (Fig. 3c) shows that  $\mathbf{n}$  aligns with the  $\rho A$  ridges, suggesting that the director tends to align with the direction of maximum stretching<sup>17</sup>. The entire time evolution of  $\mathbf{n}$  and  $\rho A$  is shown in Supplementary Video 3 (middle). Interestingly,  $+1/2$  defects appear to be in regions of low Lagrangian stretching or shearing deformation as quantified by the FTLE field. By contrast, the Lagrangian folding measure is maximum at the defects (Fig. 3d), where the absolute folding field  $|\kappa_{t_0}^t(\mathbf{x}_t, \boldsymbol{\xi}_2)|$  is superimposed to the nematic director  $\mathbf{n}$  at the same time as that in Fig. 3a.

To further quantify our observations on deformations at defects and the correlation of their dynamics with the FTLE  $\rho A$ , next we turn to numerical simulations of an incompressible ( $\nabla \cdot \mathbf{v} = 0$ ) planar uniaxial

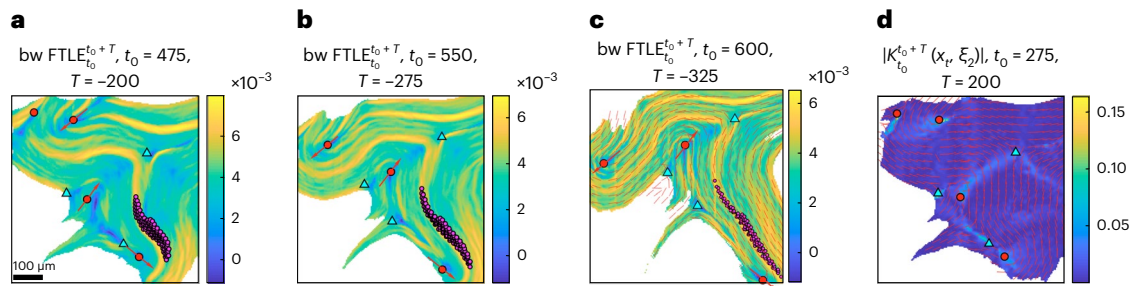


**Fig. 3 | Dynamics of an extensile active suspension of microtubule bundles and kinesin at an oil-water interface with a 2  $\mu\text{M}$  ATP concentration.** **a**,  $\nu A$  for  $|T| = 200$  s along with the position of tracers (magenta) attracted to a  $\nu A$  ridge and initially released from a circular blob. **b, c**, Same as **a** but for larger  $|T|$ . The red arrows illustrate  $+1/2$  defects pulling at the attracting  $\nu A$  ridges that, in turn, shape the Lagrangian particle motion. **d**, Absolute folding field  $|\kappa_{t_0}^{\xi_1, \xi_2}(x_t, \xi_2)|$  for

$T = 200$  s, along with topological defects and director field at the current time  $t_0 + T$  as in **a**. Defects are invariably located at regions of high folding and low stretching or shearing Lagrangian deformation. In **c** and **d**, the director field  $\mathbf{n}$  is shown in red. Time is in seconds. The colour bar in **d** encodes the Lagrangian folding in  $1 \mu\text{m}^{-1}$ , whereas the attraction rates are shown in  $\text{s}^{-1}$ . Supplementary Video 3 shows the time evolution of  $\nu A$  and  $\nu A$  along with particle motions.

active nematic liquid crystal whose dynamics are given by the nematodynamic equations

$$\rho \frac{d\mathbf{v}}{dt} = -\nabla p + \eta \nabla^2 \mathbf{v} + \nabla \cdot (\boldsymbol{\sigma}^e + \boldsymbol{\sigma}^a), \quad (6a)$$

$$\frac{d\mathbf{Q}}{dt} = \lambda \mathbf{S} \mathbf{D} + \mathbf{Q} \boldsymbol{\Omega} - \boldsymbol{\Omega} \mathbf{Q} + \gamma^{-1} \mathbf{H}, \quad (6b)$$

which can be derived from phenomenological arguments or microscopic models, and capture typical experimental statistics<sup>15</sup>. Here  $\rho$  and  $\eta$  denote the density and viscosity of the nematic fluid, respectively;  $d/dt = \partial_t + \mathbf{v} \cdot \nabla$  is the material derivative;  $\lambda$  is the flow alignment parameter; and  $\gamma$  is the rotational viscosity<sup>28</sup>. In equation (6b),  $\mathbf{Q} = S(\mathbf{n} \otimes \mathbf{n} - \mathbf{I}/2)$  denotes the nematic tensor,  $0 \leq S \leq 1$  is the nematic order parameter,  $\mathbf{I}$  is the identity tensor,  $\mathbf{D} = [\nabla \mathbf{v} + (\nabla \mathbf{v})^T]/2$  is the symmetric part and  $\boldsymbol{\Omega} = [\nabla \mathbf{v} - (\nabla \mathbf{v})^T]/2$  is the antisymmetric part of the velocity gradient  $\nabla \mathbf{v}$ .  $\mathbf{H} = -\delta F/\delta \mathbf{Q} = K \nabla^2 \mathbf{Q}^2 - (a_2 + a_4 |\mathbf{Q}|^2) \mathbf{Q}$  is the molecular tensor governing the relaxation dynamics of the nematic phase defined as the variational derivative of the two-dimensional Landau-De Gennes free energy  $F = \int f dA$ , where  $f$ , the free-energy density, is<sup>28</sup>

$$f = \frac{1}{2} K |\nabla \mathbf{Q}|^2 + \frac{1}{2} a_2 |\mathbf{Q}|^2 + \frac{1}{4} a_4 |\mathbf{Q}|^4, \quad (7)$$

where  $|\cdot|$  denotes the Frobenius norm (that is,  $|\mathbf{Q}|^2 = Q_{ij} Q_{ij}$ ),  $K$  is the orientational stiffness relating the elastic free energy to spatial inhomogeneities in the configuration of the nematic tensor and  $a_2$  and  $a_4$  are the bulk moduli. Finally,  $\boldsymbol{\sigma}^e = -\lambda \mathbf{S} \mathbf{H} + \mathbf{Q} \mathbf{H} - \mathbf{H} \mathbf{Q}$  denotes the elastic stress arising from a departure from the lowest free-energy configuration and  $\boldsymbol{\sigma}^a = \alpha \mathbf{Q}$  is the contractile ( $\alpha > 0$ ) or extensile ( $\alpha < 0$ ) active stress exerted by the active particles along  $\mathbf{n}$ . We nondimensionalize distances by the length scale  $\ell = L/5$ , where  $L$  is the system size, time by the viscous timescale  $\tau = \rho \ell^2/\eta$  and energy by  $\varepsilon = K$ . Since the typical Reynolds number of microtubules/kinesin suspensions varies in the range of  $10^{-5}$ – $10^{-3}$  depending on the ATP concentration, we eliminate the convective derivative in equation (6a) and numerically integrate equations (6a) and (6b) using finite differences on a  $128 \times 128$  collocated grid with periodic boundary conditions. Following<sup>15</sup>, we select our parameters so that the nematodynamic flows are turbulent and show that our results apply even to chaotic regimes. In all our simulations, we set the parameter values as follows:  $\lambda = 0.1$ ,  $K = 1$ ,  $a_2 = -1$ ,  $a_4 = 2$ ,  $\gamma = 10$ ,  $\alpha = -25$  and  $L = 5$ , in previously defined rescaled units (Supplementary Section 3 provides the selection of parameters). This yields the velocity field  $\mathbf{v}$  along with the nematic tensor field  $\mathbf{Q}$ , from which we identify the topological defects

(Supplementary Section 4). Our results apply to both contractile and extensile cases. We show extensile experimental and numerical datasets in the main text and contractile active nematics in the Supplementary Information.

Figure 4a–c shows  $\nu A$  for different time intervals  $|T|$ , along with the position of an initially circular set of particles (magenta) that are attracted to a  $\nu A$  ridge. Analogous to our results of the analysis of the experiments, we find that  $\nu A$  ridges are pulled (red arrows) and shaped by moving Eulerian  $+1/2$  defects and remain insensitive to  $-1/2$  defects (Fig. 4a–c). In Supplementary Section 4 and Supplementary Fig. 3, we quantify the correlation between the evolution of  $\nu A$  and defect motion. We first find a velocity field that transports and deforms  $\nu A$  over increasing  $T$ , and evaluate it at defects. The  $\nu A$  evolution along with defect velocities are provided in Supplementary Video 5. We then compute the relative angle between the  $\nu A$  velocity at defects and defects velocities. The mean and standard deviation of the relative angle associated with positive defects are six times smaller compared to those related to negative defects. We perform the same analysis on the experimental data in Fig. 3 and find that the mean and standard deviation of the relative angle associated with positive defects are three and four times smaller, respectively, compared with those related to negative defects (Supplementary Section 4). Supplementary Video 6 is similar to Supplementary Video 5 but for the experimental data. We note that  $\nu A$  is Lagrangian, that is, it contains information of particle trajectories, whereas defects are Eulerian and hence agnostic to particle paths. This connection could provide a quantitative framework to control the Lagrangian motion and deformation of active nematics by steering the position of Eulerian defects.

As in Fig. 3c, Fig. 4c shows that  $\mathbf{n}$  tends to align with attracting  $\nu A$  ridges. By contrast, in contractile active nematics simulated using equations (6a) and (6b) with the same parameters of the extensile case and  $\alpha = 25$ , we find that  $\mathbf{n}$  tends to be perpendicular to attracting  $\nu A$  ridges (Supplementary Section 5 and Supplementary Fig. 4). In Supplementary Section 6 and Supplementary Fig. 5, we perform the same analysis as that in Fig. 4 on simulated extensile active nematic in confined geometry characterized by dancing defects<sup>29</sup> and find again that  $\mathbf{n}$  tends to align with attracting  $\nu A$  ridges, consistent with Figs. 3c and 4c. In Supplementary Section 7 and Supplementary Fig. 6, we provide a mechanistic argument that explains these observations. First, we show that in extensile (contractile) nematics,  $\mathbf{n}$  tends to align with (perpendicular to) the leading eigenvector  $\mathbf{e}_2$  of  $\mathbf{D}$ . This provides a precise connection between  $\mathbf{n}$  and Eulerian—or short-time—attractors (repellers)<sup>19</sup>, which are parallel (perpendicular) to  $\mathbf{e}_2$ . Then, we relate  $\mathbf{n}$  to Lagrangian attractors.

In Supplementary Section 8 and Supplementary Fig. 7, we also provide an aggregate measure of positional coherence by

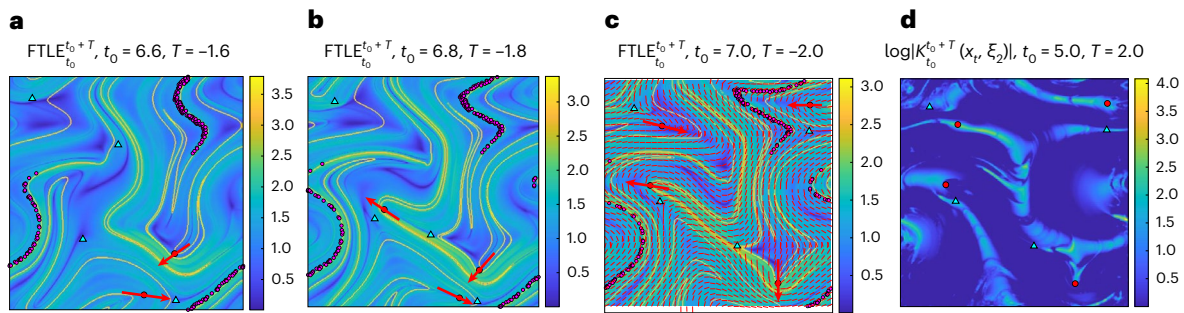


**Fig. 4 | Lagrangian analysis of a simulated extensile active nematic fluid.** The nematic fluid obeys equations (6a) and (6b). **a**,  $\nu A$  for  $|T| = 1.6$ , along with the position of material particles (magenta) attracted to a  $\nu A$  ridge and initially released from a circular blob. **b, c**, Same as **a**, but for larger  $|T|$ . The red arrows illustrate that  $+1/2$  defects pull the attracting  $\nu A$  ridges that, in turn, shape particle

motion. In **c**, the red segments display the director field. **d**, Logarithm of the folding field modulus  $|K_{t_0}^{t_0+T}(x_t, \xi_2)|$  for  $T = 2$ , as that in **c**. Supplementary Video 4 shows the evolution of the data in **a** and **d** for different  $T$  values. The positive defects are located at regions of high folding and low stretching or shearing Lagrangian deformation.

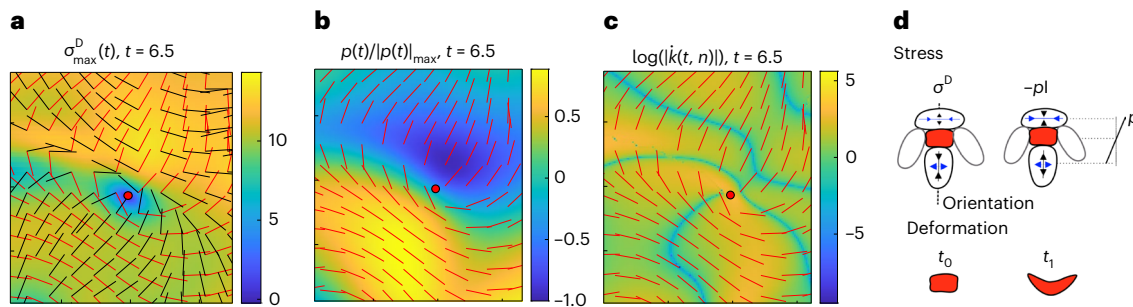


**Fig. 5 | Stress and deformation around an isolated  $+1/2$  defect in simulated extensile active nematics.** **a**, Maximum eigenvalue of the total deviatoric stress  $\sigma^D$  in the proximity of a  $+1/2$  defect (red circle). The leading eigenvector of  $\sigma^D$  is marked by black lines and the the nematic director field, by red lines (Supplementary Fig. 10 shows separate viscous, elastic and active stress contributions). **b**, Pressure field normalized by its maximum absolute value characterizes the isotropic stress  $\sigma^I = -pl$ . **c**, Logarithm of the folding rate

modulus of the active nematic, computed from equation (8). **d**, Sketch of the deviatoric and isotropic stress distribution near an isolated  $+1/2$  defect in extensile active nematics (top). The arrow size is proportional to the stress level, and the blue arrow marks the direction perpendicular to defect orientation. A sketch of the material deformation near a  $+1/2$  defect (bottom). Supplementary Fig. 9 shows the equivalent analysis for the contractile case.

using the inverse of the broadly used  $H^{-1}$  mixing norm<sup>30</sup>, and show how it decreases with increasing integration time  $T$  and activity  $\alpha$ . Our results are consistent with<sup>17</sup> where it was discovered that in the asymptotic limit  $T \rightarrow \infty$ , the braiding of positive defects contributes dominantly to the increase in topological entropy in active nematics. However, although<sup>17</sup> quantifies the contribution of  $+1/2$  defects to the aggregate (that is, space-independent) mixing, here we focus and uncover dynamic spatial structures (attracting Lagrangian CSs) that shape particle motion while being steered by  $+1/2$  defects. In other words, we identify the spatiotemporal organizer of active nematics that complement previous analyses of global mixing properties. Figure 4d shows  $\kappa_{t_0}^t(x_t, \xi_2)$  associated with  $|T| = 2$  (Fig. 4c). Consistent with our experimental results (Fig. 3), we see that  $+1/2$  defects are preferentially located in regions of high Lagrangian folding and low stretching. We obtain results similar to Fig. 4 for contractile ( $\alpha > 0$ ) active nematics, simulated using the same parameters listed above and  $\alpha = 25$  (Supplementary Section 5). Supplementary Video 7 shows the same data as Supplementary Video 4 but for the contractile case. Finally, in Supplementary Section 9 and Supplementary Fig. 8, we confirm that Lagrangian structures contained in  $\nu A$  and  $\kappa$  remain typically inaccessible to Eulerian quantities such as the director field  $\mathbf{n}$ , the nematic order parameter  $S$ , the eigenvalues and eigenvectors of the rate-of-strain tensor, the velocity divergence  $\nabla \cdot \mathbf{v}$ , and bend and splay elastic energies.

**Stress gradients are maximum at positive defects**

Motivated by the striking deformations associated with  $+1/2$  defects, we analyse the stress distribution using the simulation data for extensile active nematics in Fig. 4. We find that the magnitude of both deviatoric and isotropic total stresses are minimum at  $+1/2$  defects, but their gradients have high values at these locations along the defect orientation (Fig. 5a,b), and thus induces folding deformation (Fig. 5d). We obtain similar results for contractile active nematics (Supplementary Section 10 and Supplementary Fig. 9), where the folding direction is towards the head of the defect as opposed to the tail (Fig. 5d).

To bridge the gap between the Lagrangian deformations, which accounts for the motion history of the nematic continuum, and Eulerian deformations based on an instantaneous configuration, we derived an exact formula for the Eulerian folding rate

$$\dot{\kappa}(t, \mathbf{x}, \mathbf{n}) = [(\mathbf{VD}(\mathbf{x}, t)\mathbf{n}) \cdot \mathbf{n}_\perp - \frac{\nabla \omega(\mathbf{x}, t) \cdot \mathbf{n}}{2}] \quad (8)$$

experienced by an infinitesimal patch of nematic fluid with orientation  $\mathbf{n}$  (Supplementary Section 1). The folding rate can be computed from  $\mathbf{v}$  and  $\mathbf{n}$ , and arises from spatial heterogeneities of the rate-of-strain tensor  $\mathbf{D}$  and vorticity  $\omega$ . For example, if the nematic continuum is an epithelium,  $\dot{\kappa}(t, \mathbf{x}, \mathbf{n})$  measures the bending rate experienced by the cell located at  $\mathbf{x}$  with orientation  $\mathbf{n}$ . Using equation (8), we also find

that  $k(t, \mathbf{x}, \mathbf{n})$  is the maximum in the vicinity of +1/2 defects (Fig. 5c), consistent with the corresponding stress distribution (Fig. 5a,b) and Lagrangian folding (Fig. 4).

It is interesting to compare these results with experimental findings that suggest a biological consequence of topological defects in epithelial layers<sup>12,31,32</sup>, where the deformations and stress at the defects is thought to elucidate how mechanical stimuli are converted into downstream biochemical signals. Positive defects with strength +1/2 in monolayers of Madin–Darby canine kidney cells, for example, have been associated with sites of cell apoptosis<sup>31</sup>, with a possible explanation being the high compressive stress at the defect location. This hypothesis has been tested by correlating the isotropic stress averaged over several (~6) cell sizes in the neighbourhood of a topological defect during apoptosis<sup>31</sup>. Our findings, however, show that bending deformations are dominant at positive defects, suggesting that there may be other mechanisms at play associated with bending deformations at topological defects.

We observe a clear similarity of the extensile active nematic stress distribution (Fig. 5) with that experimentally measured in monolayers of Madin–Darby canine kidney cells<sup>31</sup> during apoptosis. It is worth noting that the novel stress and deformation distribution around +1/2 defects, together with the known ability of cells to sense curvature changes<sup>33</sup>, may lead to uncovering new feedback mechanisms in active epithelial dynamics<sup>34,35</sup>.

## Discussion

By combining concepts from nonlinear dynamics, experiments on two-dimensional active nematics, and simulations of active nematodynamics equations, we found that the motion of active nematics is organized by dynamic (time-dependent) attracting and repelling CSs, whose motion is coupled to that of +1/2 topological defects. As the defects move, they deform attracting CSs, which in turn regulate collective motion. Furthermore, the Lagrangian timescale-dependent maps of stretching- and folding-type deformations of a nematic continuum show that +1/2 defects are correlated with locations of high bending and low stretching-type or shearing-type deformations. Motivated by this finding, we have discovered a characteristic stress distribution around +1/2 defects: the stress is the minimum at the defect, but its large gradient along the defect's orientation causes differential stress that induces bending. The bending is towards the defect head (tail) for contractile (extensile) active nematics. Similar stress distributions were experimentally measured in monolayers of Madin–Darby canine kidney cells<sup>31</sup>. Finally, we have observed and explained that the nematic director tends to align along (perpendicular to) attracting Eulerian and Lagrangian CSs<sup>18,19</sup> for extensile (contractile) active nematics.

More broadly, using only the measured velocity and nematic director, our results provide a quantitative framework for assessing the motion, mixing and deformation of active nematics. Emerging experimental evidence associates biological functionality with topological defects of cells orientation<sup>12</sup>, actin fibre orientation<sup>36</sup> and the ability of cells to sense and react to bending and stretching deformations<sup>33</sup>. From this perspective, our approach quantifies the stretching and folding deformations in a nematic continuum as timescale-dependent maps. Investigating the correlation between curvature and stretching deformation maps in epithelial layers and other similar systems could elucidate how cells couple mechanical inputs to intracellular signals in oriented active matter systems.

## Online content

Any methods, additional references, Nature Portfolio reporting summaries, source data, extended data, supplementary information, acknowledgements, peer review information; details of author contributions and competing interests; and statements of data and code availability are available at <https://doi.org/10.1038/s41567-023-02062-y>.

## References

- Vicsek, T. & Zafeiris, A. Collective motion. *Phys. Rep.* **517**, 71–140 (2012).
- Marchetti, M. C. et al. Hydrodynamics of soft active matter. *Rev. Mod. Phys.* **85**, 1143–1189 (2013).
- Kruse, K., Joanny, J., Jülicher, F., Prost, J. & Sekimoto, K. Asters, vortices, and rotating spirals in active gels of polar filaments. *Phys. Rev. Lett.* **92**, 078101 (2004).
- Ballerini, M. et al. Interaction ruling animal collective behavior depends on topological rather than metric distance: evidence from a field study. *Proc. Natl Acad. Sci. USA* **105**, 1232–1237 (2008).
- Zhang, H., Ber, A., Florin, E. & Swinney, H. Collective motion and density fluctuations in bacterial colonies. *Proc. Natl Acad. Sci. USA* **107**, 13626–13630 (2010).
- Bricard, A., Caussin, J., Desreumaux, N., Dauchot, O. & Bartolo, D. Emergence of macroscopic directed motion in populations of motile colloids. *Nature* **503**, 95–98 (2013).
- Dombrowski, C., Cisneros, L., Chatkaew, S., Goldstein, R. & Kessler, J. Self-concentration and large-scale coherence in bacterial dynamics. *Phys. Rev. Lett.* **93**, 098103 (2004).
- Copenhagen, K., Alert, R., Wingreen, N. S. & Shaevitz, J. W. Topological defects promote layer formation in *Myxococcus xanthus* colonies. *Nat. Phys.* **17**, 211–215 (2021).
- Meacock, O. J., Doostmohammadi, A., Foster, K. R., Yeomans, J. M. & Durham, W. M. Bacteria solve the problem of crowding by moving slowly. *Nat. Phys.* **17**, 205–210 (2021).
- Fiedl, P. & Gilmour, D. Collective cell migration in morphogenesis, regeneration and cancer. *Nat. Rev. Mol. Cell Biol.* **10**, 445–457 (2009).
- Ladoux, B. & Mège, R. Mechanobiology of collective cell behaviours. *Nat. Rev. Mol. Cell Biol.* **18**, 743–757 (2017).
- Doostmohammadi, A., Ignés-Mullol, J., Yeomans, J. & Sagués, F. Active nematics. *Nat. Commun.* **9**, 3246 (2018).
- Serra, M., Streichan, S., Chuai, M., Weijer, C. J. & Mahadevan, L. Dynamic morphoskeletons in development. *Proc. Natl Acad. Sci. USA* **117**, 11444–11449 (2020).
- Wensink, H. et al. Meso-scale turbulence in living fluids. *Proc. Natl Acad. Sci. USA* **109**, 14308–14313 (2012).
- Giomi, L. Geometry and topology of turbulence in active nematics. *Phys. Rev. X* **5**, 031003 (2015).
- Shankar, S. & Marchetti, M. C. Hydrodynamics of active defects: from order to chaos to defect ordering. *Phys. Rev. X* **9**, 041047 (2019).
- Tan, A. J. et al. Topological chaos in active nematics. *Nat. Phys.* **15**, 1033–1039 (2019).
- Haller, G. Lagrangian coherent structures. *Annu. Rev. Fluid Mech.* **47**, 137–162 (2015).
- Serra, M. & Haller, G. Objective Eulerian coherent structures. *Chaos* **26**, 053110 (2016).
- Hadjighasem, A., Farazmand, M., Blazeviski, D., Froyland, G. & Haller, G. A critical comparison of Lagrangian methods for coherent structure detection. *Chaos* **27**, 053104 (2017).
- Serra, M., Sathe, P., Beron-Vera, F. & Haller, G. Uncovering the edge of the polar vortex. *J. Atmos. Sci.* **74**, 3871–3885 (2017).
- Serra, M. et al. Search and rescue at sea aided by hidden flow structures. *Nat. Commun.* **11**, 2525 (2020).
- Nolan, P. J., Serra, M. & Ross, S. D. Finite-time Lyapunov exponents in the instantaneous limit and material transport. *Nonlinear Dyn.* **100**, 3825–3852 (2020).
- Truesdell, C. & Noll, W. *The Non-Linear Field Theories of Mechanics* (Springer, 2004).
- Giona, M. & Adrover, A. Nonuniform stationary measure of the invariant unstable foliation in Hamiltonian and fluid mixing systems. *Phys. Rev. Lett.* **81**, 3864 (1998).
- Serra, M., Vétel, J. & Haller, G. Exact theory of material spike formation in flow separation. *J. Fluid Mech.* **845**, 51–92 (2018).

27. Sanchez, T., Chen, D., DeCamp, S., Heymann, M. & Dogic, Z. Spontaneous motion in hierarchically assembled active matter. *Nature* **491**, 431–434 (2012).
28. De Gennes, P. & Prost, J. *The Physics of Liquid Crystals* 2nd edn (Oxford Univ. Press, 1993).
29. Shendruk, T. N., Doostmohammadi, A., Thijssen, K. & Yeomans, J. M. Dancing disclinations in confined active nematics. *Soft Matter* **13**, 3853–3862 (2017).
30. Doering, C. R. & Thiffeault, J.-L. Multiscale mixing efficiencies for steady sources. *Phys. Rev. E* **74**, 025301 (2006).
31. Saw, T. et al. Topological defects in epithelia govern cell death and extrusion. *Nature* **544**, 212–216 (2017).
32. Kawaguchi, K., Kageyama, R. & Sano, M. Topological defects control collective dynamics in neural progenitor cell cultures. *Nature* **545**, 327–331 (2017).
33. Dreher, D., Pasakarnis, L. & Brunner, D. Snapshot: mechanical forces in development II. *Cell* **165**, 1028–1028 (2016).
34. Aragona, M. et al. A mechanical checkpoint controls multicellular growth through YAP/TAZ regulation by actin-processing factors. *Cell* **154**, 1047–1059 (2013).
35. Balasubramaniam, L. et al. Investigating the nature of active forces in tissues reveals how contractile cells can form extensile monolayers. *Nat. Mater.* **20**, 1156–1166 (2021).
36. Maroudas-Sacks, Y. et al. Topological defects in the nematic order of actin fibres as organization centres of hydra morphogenesis. *Nat. Phys.* **17**, 251–259 (2021).

**Publisher's note** Springer Nature remains neutral with regard to jurisdictional claims in published maps and institutional affiliations.

Springer Nature or its licensor (e.g. a society or other partner) holds exclusive rights to this article under a publishing agreement with the author(s) or other rightsholder(s); author self-archiving of the accepted manuscript version of this article is solely governed by the terms of such publishing agreement and applicable law.

© The Author(s), under exclusive licence to Springer Nature Limited 2023

## Methods

### Experimental data

We discuss our microtubule-based active nematic experiments in detail in Supplementary Section 2.

### Numerical data

We solve our active nematodynamic equations using a dedicated code developed elsewhere<sup>15</sup>.

### FTLE, Lagrangian folding and Eulerian folding rates

Given a modelled or experimental planar velocity field  $\mathbf{v}(\mathbf{x}, t)$ , we compute the Lagrangian attractors and repellers from backward and forward FTLE (equation (3)). To compute the FTLE, we first calculate  $\mathbf{F}_{t_0}^t(\mathbf{x}_0)$  (equation (1)) by integrating the cell velocity field  $\mathbf{v}(\mathbf{x}, t)$  using the built-in Runge–Kutta solver ODE45 in MATLAB 2021b with absolute and relative tolerance of  $10^{-6}$ , linear interpolation in space and time and a uniform dense grid of initial conditions. Then, we compute  $\nabla\mathbf{F}_{t_0}^t(\mathbf{x}_0)$  taking the spatial derivatives of  $\mathbf{F}_{t_0}^t(\mathbf{x}_0)$  with respect to the initial conditions using centred finite-difference approximation. Using equation (2), we compute  $\mathbf{C}_{t_0}^t(\mathbf{x}_0)$  and use the eigenvalue MATLAB function to calculate its largest eigenvalue field  $\lambda_2$  and the corresponding eigenvector field  $\boldsymbol{\xi}_2$ . Using numerical centred finite differencing, we calculate the second spatial derivatives of  $\mathbf{F}_{t_0}^t(\mathbf{x}_0)$  and compute the Lagrangian folding field  $\kappa$  from equation (4). Using the same numerical schemes, we compute the Eulerian folding rate field  $\dot{\kappa}$  (equation (8)).

### Topological defects

We discuss the identification of topological defects, calculation of defect velocity and their correlation with the motion of Lagrangian attractors in detail in Supplementary Section 4.

### Data availability

The experimental and simulated data that support the findings of this study are available from the corresponding authors upon request.

### Code availability

The codes used in this work are available from the corresponding authors upon request.

## Acknowledgements

We acknowledge T. N. Shendruk, A. Doostmohammadi, K. Thijssen and J. M. Yeomans for providing the dataset<sup>29</sup> analysed in Supplementary Fig. 3. We are grateful to S. Shankar and N. Molinari for helpful discussions. This work is partially supported by the Schmidt Science Fellowship and the Postdoc Mobility Fellowship from the Swiss National Foundation (M.S.); the Netherlands Organization for Scientific Research (NWO/OCW) as part of the Frontiers of Nanoscience program and the Vidi scheme (L.G.); the Department of Energy, Office of Basic Energy Sciences, under award no. DESC0019733 (Z.D.); and the NSF Simons Center for Mathematical and Statistical Analysis of Biology via award no. 1764269 (L.M.).

## Author contributions

M.S. and L.M. designed research, M.S. performed the research. M.S., L.L., L.G., Z.D. and L.M. contributed to the new experimental, numerical and analytical tools. M.S., L.L., L.G., Z.D. and L.M. analysed the data, and M.S. and L.M. wrote the manuscript. All authors commented on the manuscript.

## Competing interests

The authors declare no competing interests.

## Additional information

**Supplementary information** The online version contains supplementary material available at <https://doi.org/10.1038/s41567-023-02062-y>.

**Correspondence and requests for materials** should be addressed to Mattia Serra or L. Mahadevan.

**Peer review information** *Nature Physics* thanks the anonymous reviewers for their contribution to the peer review of this work

**Reprints and permissions information** is available at [www.nature.com/reprints](http://www.nature.com/reprints).



# Defect-mediated dynamics of coherent structures in active nematics

---

In the format provided by the authors and unedited

---

# Contents

S1 Lagrangian folding and Eulerian folding rates	2
S2 Experimental data	2
S3 Parameter selection for numerical simulations	5
S4 Positive defects move and deform attracting Lagrangian coherent structures	5
S5 Contractile active nematics	6
S6 Analysis of the dancing disclinations flow in confined active nematics	7
S7 Relative orientation between $\mathbf{n}$ , $\mathbf{e}_2$ and attracting coherent structures	8
S8 Positional coherence as a function of time and activity	9
S9 Lagrangian vs Eulerian quantities	11
S10 Stress at $+1/2$ defects	13

# S1 Lagrangian folding and Eulerian folding rates

The curvature of an infinitesimal material fiber at time  $t$  starting from the initial position  $\mathbf{x}_0$ , with an orientation  $\theta$ , and curvature  $\kappa_0$ , due to the transport and deformation induced by the flow map  $\mathbf{F}_{t_0}^t(\mathbf{x}_0)$ , can be computed<sup>1</sup> as

$$\begin{aligned} \kappa_{t_0}^t : \mathbb{R}^2 \times \mathbb{S}^1 \times \mathbb{R} &\rightarrow \mathbb{R}, \\ \kappa_{t_0}^t(\mathbf{x}_0, \theta, \kappa_0) &= \frac{[(\nabla^2 \mathbf{F}_{t_0}^t(\mathbf{x}_0) \mathbf{e}_\theta) \mathbf{e}_\theta] \cdot [\mathbf{R} \nabla \mathbf{F}_{t_0}^t(\mathbf{x}_0) \mathbf{e}_\theta]}{(\mathbf{e}_\theta \cdot [\mathbf{C}_{t_0}^t(\mathbf{x}_0) \mathbf{e}_\theta])^{3/2}} + \kappa_0 \frac{\det[\nabla \mathbf{F}_{t_0}^t(\mathbf{x}_0)]}{(\mathbf{e}_\theta \cdot [\mathbf{C}_{t_0}^t(\mathbf{x}_0) \mathbf{e}_\theta])^{3/2}}, \end{aligned} \quad (\text{S1})$$

where  $\mathbf{e}_\theta = [\cos \theta, \sin \theta]$  and  $(\nabla^2 F_{t_0}^t(\mathbf{x}_0) e_{\theta_k})_{ij} = \sum_k F_{t_0 i, jk}^t(\mathbf{x}_0) e_{\theta_k}$ ,  $i, j, k \in \{1, 2\}$  and  $\mathbf{R}$  denotes a counterclockwise ninety-degree rotation matrix. By evaluating  $\kappa_{t_0}^t(\mathbf{x}_0, \theta, \kappa_0)$  for an initially straight ( $\kappa_0 = 0$ ) fiber aligned with the dominant eigenvector of  $\mathbf{C}_{t_0}^t$  ( $\mathbf{e}_\theta = \xi_2$ ), we obtain Eq. (4) in the main text.

In the instantaneous limit ( $t = t_0$ ), the material curvature rate of the material fiber<sup>1</sup> is given by

$$\begin{aligned} \left. \frac{d\kappa_{t_0}^t(\mathbf{x}_0, \theta, \kappa_0)}{dt} \right|_{t=t_0} &= \dot{\kappa}_{t_0}(\mathbf{x}_0, \theta, \kappa_0) \\ &= [(\nabla \mathbf{D}(\mathbf{x}_0, t_0) \mathbf{e}_\theta) \mathbf{e}_\theta] \cdot \mathbf{R} \mathbf{e}_\theta - \frac{\nabla \omega(\mathbf{x}_0, t_0) \cdot \mathbf{e}_\theta}{2} + \kappa_0 \left[ \nabla \cdot \mathbf{v}(\mathbf{x}_0, t_0) - 3 \mathbf{e}_\theta \cdot [\mathbf{D}(\mathbf{x}_0, t_0) \mathbf{e}_\theta] \right], \end{aligned} \quad (\text{S2})$$

where  $\mathbf{D}$  denotes the rate-of-strain tensor,  $\omega$  the vorticity,  $\nabla \cdot \mathbf{v}$  the divergence of the flow and  $(\nabla D(\mathbf{x}_0, t_0) e_{\theta_k})_{ij} = \sum_k D_{ij,k}(\mathbf{x}_0) e_{\theta_k}$ ,  $i, j, k \in \{1, 2\}$ . Integrating Eq. (S2) along trajectories  $\mathbf{F}_{t_0}^t(\mathbf{x}_0)$ , provides an alternative formula to compute Eq. (S1) from known Eulerian quantities (see Eq. B1 in<sup>1</sup>). Evaluating eq. (S2) along the current nematic director ( $\mathbf{e}_\theta \equiv \mathbf{n}$ ), and assuming  $\kappa_0 \equiv 0$ , one can compute the instantaneous folding rate experienced by a nematic continuum using only the velocity and the director fields inputs as

$$\dot{\kappa}(t, \mathbf{x}, \mathbf{n}) = [(\nabla \mathbf{D}(\mathbf{x}, t) \mathbf{n}) \mathbf{n}] \cdot \mathbf{n}_\perp - \frac{\nabla \omega(\mathbf{x}, t) \cdot \mathbf{n}}{2}, \quad (\text{S3})$$

where  $\mathbf{n}_\perp = \mathbf{R} \mathbf{n}$ . We note that eq. (S3) allows quantifying the folding rate contribution coming from spatial inhomogeneities of the rate of strain tensor and the vorticity. To deploy these results in an experimental setting, consider a nematic continuum that describes an epithelial tissue where  $\mathbf{n}$  represents the cell orientation field. Then, for instance, eq. (S3) quantifies the instantaneous bending rate of epithelial cells assuming that cells have initially zero curvature.

## S2 Experimental data

### Velocity and Orientation Fields

We prepared a microtubule-based active nematic at 1.4 mM ATP doped with a small fraction of Alexa-647 labeled MTs<sup>2;3</sup>. We imaged the sample both using LC-PolScope and epifluorescence microscopy. LC-PolScope provides a direct measurement of the orientation field of the MTs<sup>4</sup>. Particle image velocimetry was used to find the velocity field from the fluorescence images. The

LC-PolScope and fluorescence images were taken sequentially within 2s of each other; however, we treat the lag as negligible in the data as calculating the velocity field coarse grains the data in time. Imaging was done on a Nikon Ti Eclipse equipped with Andor Neo camera and LC-PolScope device.

Importantly, we optimized the experimental conditions for particle image velocimetry analysis. In a test data set, we labeled a sample with two colors of fluorescent microtubules and concurrently imaged both channels [Fig S1(a)]. In one color, nearly all the microtubules (1 mg/mL) were labeled, leading to the classic fingerprint pattern in an active nematic [Fig S1(b)]. In the other color, only 1 in every 10,000 microtubules was labeled, leading to a speckle pattern [Fig. S1(b)]. We performed PIV on both image sequences and obtained smooth and visually reasonable resulting flow fields [Fig. S1(d)(e)]. However, the detailed structures of the flow are lost in the fully labeled nematic flow field, such as the vortex caused by two rotating plus 1/2 [Fig. S1 (a)(e)]. We hypothesized that PIV underestimated the velocities along the director in the fully labeled nematic due to the relatively uniform fluorescence in that direction. To verify this, we obtained the orientation field of the microtubules from OrientationJ on the fully labeled images which finds the eigenvector of the structure tensor. We then decomposed the velocity into components along the director  $u_n$  and perpendicular to the director  $u_m$ . The resulting histograms show a bias in the fully labeled flow fields, in which  $u_n$  is systematically lower than  $u_m$  [Fig. S1 (f)]. In comparison, the histogram of velocities from the speckle labeled images Fig. S1 (d) show no systematic bias. The underestimation of speeds along the director also impacts the average speed of the material, with the fully labeled fluorescence underestimating the speed compared to the speckle labeled analysis [Fig. S1 (h)]. For this reason, we used sparsely labeled nematics to measure flow fields using PIV throughout the study.

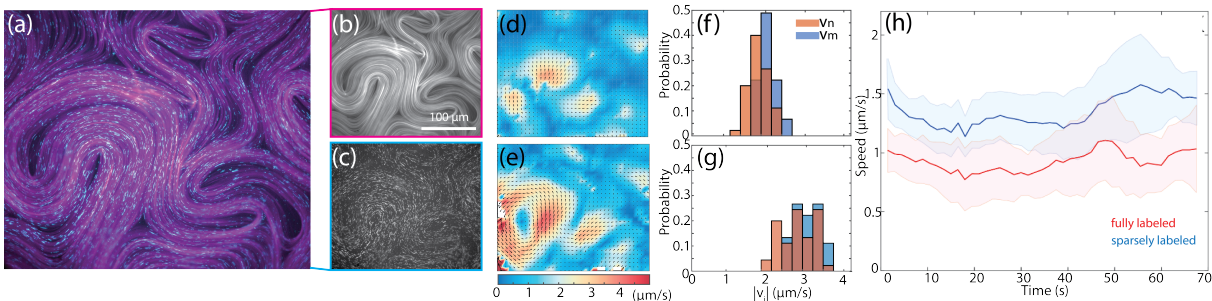


Figure S1: Speckle labeling optimizes particle image velocimetry (PIV) analysis. (a) Alexa 647 labeled microtubules at 1 mg/mL and Alexa 488 labeled microtubules at  $<1 \mu\text{g/mL}$  in an active nematic. (b) The fully labeled fluorescence image. (c) The speckle labeled fluorescence image. (d) The flow field measured from PIV on (b). (e) The flow field measured from PIV on (c). (f) Histograms of the magnitude of the velocity components along the director  $v_n$  (orange) and perpendicular to the director  $v_m$  (blue) from the fully labeled PIV analysis (b)(d). (g) Histograms of the magnitude of the velocity components along the director  $v_n$  (orange) and perpendicular to the director  $v_m$  (blue) from the speckle labeled PIV analysis (c)(e). (h) A comparison of the average speed over time from the fully labeled (b)(d)(f) and speckle labeled (c)(e)(g) image analyses.

Lastly, as additional validation we note that a side-by-side analysis of PIV velocity on microtubules and bead velocities shows overlapping histograms of speed distribution as well as nearly identical curves of average speed over time (Fig. 12 in<sup>5</sup>).

## Photobleaching

We prepared microtubule-based active nematic at  $18\mu\text{M}$  ATP with Alexa-647 labeled MTs<sup>2</sup>. It was important to use a low amount of ATP to slow the dynamics so that the timescale of bleaching was faster than the movement of the material. We included a small fraction of MTs labeled with Azide-DBCO-488 to simultaneously bleach regions and measure the velocity field of the material. We used a Leica SP8 Confocal with a 20X NA 0.75 air objective to bleach and image the sample. Since Image Brightness  $\propto (\text{NA}^2/M)^2$ , bleaching is most efficient at low magnification and high NA. To bleach, we decreased the range over which the galvo-mirror scans by 20 times and turned a 633nm laser power to its maximum. With this combination, we were able to bleach in under 5 seconds so that the distortions due to material movement were minimal. Using Leica software, we were able to define regions of interest to bleach defined shapes. To image the sample we reduced the 633nm laser power to 0.5% of its maximum and simultaneously imaged with a 488nm laser.

## PIV velocity validation

We further verify the validity of our PIV-derived velocity by comparing its Lagrangian trajectories with the evolution of photo-bleached patches. We first use the image processing software Ilastik to extract photo-bleached patches from experimental images at different times. Then, we use the set of patch points at the initial time, and advect them with the PIV velocity. Because photo-bleached patches undergo advection and diffusion while those advected by PIV only advection, we compare the two using the distance between the corresponding patch centroids. [Movie8](#) and [Fig.S2a](#) show the evolution of the photo-bleached (cyan) top left patch ([Fig. 2d-f](#)) along with the corresponding one (magenta) obtained from PIV velocity (blue), confirming the validity of our PIV velocity. As an aggregate measure, we compute the average distance  $\langle d \rangle$  between the centroids of the nine photo-bleached and PIV-based patches nondimensionalized by the smaller size of our domain  $L$  over time ([Fig.S2b](#)). Our analysis quantitatively shows the validity of Lagrangian trajectories obtained by PIV velocities.

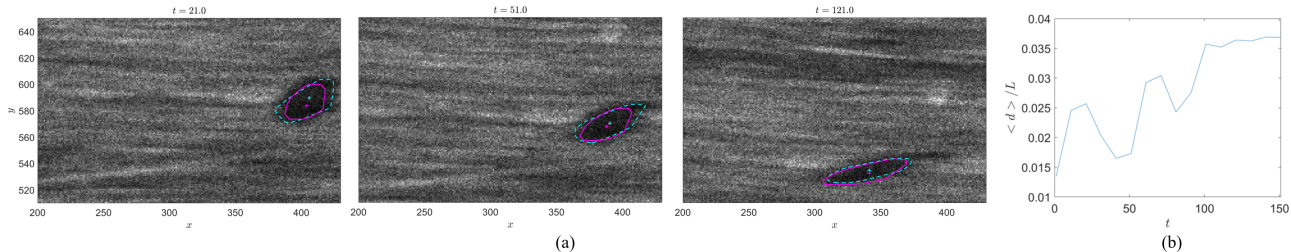


Figure S2: Validation of Lagrangian trajectories from PIV-velocities. (a) Evolution of the photo-bleached (cyan) top left patch ([Fig. 2d-f](#)) along with the corresponding one (magenta) obtained from PIV velocity. [Movie8](#) shows the complete time evolution. (b)  $\langle d \rangle$  denotes the average distance between the centroids (+ markers) of the nine photo-bleached and PIV-based patches nondimensionalized by the smaller size of our domain  $L$  over time.

### S3 Parameter selection for numerical simulations

In our numerical simulations we have made all physical quantities dimensionless by using the following units. Unit of energy  $\mathcal{E} = K$ , length  $\ell = L/5$ , and time  $\tau = \frac{\rho\ell^2}{\eta}$ . Here  $K$  is the Frank elastic constant,  $L$  the system size,  $\rho$  the fluid density and  $\eta$  the shear viscosity. As a consequence of this choice, most parameters drop from the hydrodynamic equations and do not require to be assigned a specific numerical value, with exception for the nematic order parameter  $S$ , the rotational viscosity  $\gamma$  and the flow alignment parameter  $\lambda$ .

For simplicity, we used  $S = 1$ . Furthermore, as in nematic liquid crystals  $\gamma/\eta$  ranges from 1 to  $10^3$  (see e.g.<sup>6</sup>), and in the absence of more specific experimental estimates of this quantity, we choose  $\gamma = 10\eta$ . Finally, as shown in<sup>7</sup>, the magnitude of the flow alignment parameter  $\lambda$ , which is crucial in the laminar regime and for the hydrodynamic stability of active nematics, has no visible effects in the chaotic regime. We choose  $\lambda = 0.1$ , well within the typical range of passive nematic liquid crystals (i.e.  $-1 < \lambda < 1$  although no fundamental principle prevents other values).

### S4 Positive defects move and deform attracting Lagrangian coherent structures

We quantify the influence of moving defects on the motion and deformation of attracting Lagrangian Coherent Structures identified with the backward FTLE discussed in Fig. 4. Denoting by  $\mathbf{q}(\cdot, t) := [Q_{11}(\cdot, t), Q_{12}(\cdot, t)]^\top$  the vector containing the independent entries of the nematic tensor, and by  $\mathbf{x}^d(t) := \arg \mathbf{q}(\mathbf{x}^d(t), t) = 0$  the time- $t$  position of disclinations, we compute the disclination velocities by Taylor-expanding the equation defining defect locations

$$\arg_{\mathbf{x}^d(t+\delta t)} \mathbf{q}(\mathbf{x}^d(t+\delta t), t+\delta t) \approx \arg_{\mathbf{x}^d(t)} \mathbf{q}(\mathbf{x}^d(t), t) + [\nabla \mathbf{q}(\mathbf{x}^d(t), t) \mathbf{v}^d(t) + \partial_t \mathbf{q}(\mathbf{x}^d(t), t)] \delta t = 0, \quad (\text{S4})$$

and requiring the leading order term to vanish, i.e.

$$\mathbf{v}^d(t) = -[\nabla \mathbf{q}(\mathbf{x}^d(t), t)]^{-1} \partial_t \mathbf{q}(\mathbf{x}^d(t), t). \quad (\text{S5})$$

By the implicit function theorem,  $\mathbf{v}^d(t)$  exists whenever  $[\nabla \mathbf{q}(\mathbf{x}^d(t), t)]$  is invertible. Following<sup>8</sup>, we compute the index of the disclination at  $\mathbf{x}^d$  as

$$\text{ind}_d = \frac{1}{2\pi} \sum_{i=1}^n \Delta_i, \quad \Delta_i = \phi_{i+1} - \phi_i - \pi \text{round} \left( \frac{\phi_{i+1} - \phi_i}{\pi} \right), \quad \phi_{n+1} = \phi_1, \quad (\text{S6})$$

where  $\phi_i$ ,  $i = 1, \dots, 4$  denotes the angle between the nematic director and the horizontal axis at each of the grid points surrounding the defect.

To quantify the deformation of the FTLE field with respect to  $|T|$ , we use Digital Particle Image Velocimetry to obtain a fictitious velocity field,  $\mathbf{v}_{FTLE}(\mathbf{x}, T)$ , that deforms the  $\text{FTLE}_{t_0}^{t_0-|T|}$  onto  $\text{FTLE}_{t_0+\Delta T}^{t_0-(|T|+\Delta T)}$  (Fig. S3a). Evaluating such velocity field at the current location  $\mathbf{x}^d_i(T)$  of defect  $i$ , we compute the relative angle between  $\mathbf{v}_{FTLE}$  and  $\mathbf{v}^d$  as

$$\varphi_i(T) = \arccos \frac{\mathbf{v}_{FTLE}(\mathbf{x}^d_i(T), T) \cdot \mathbf{v}^d_i(T)}{|\mathbf{v}^d_i(T)| |\mathbf{v}_{FTLE}(\mathbf{x}^d_i(T), T)|}. \quad (\text{S7})$$

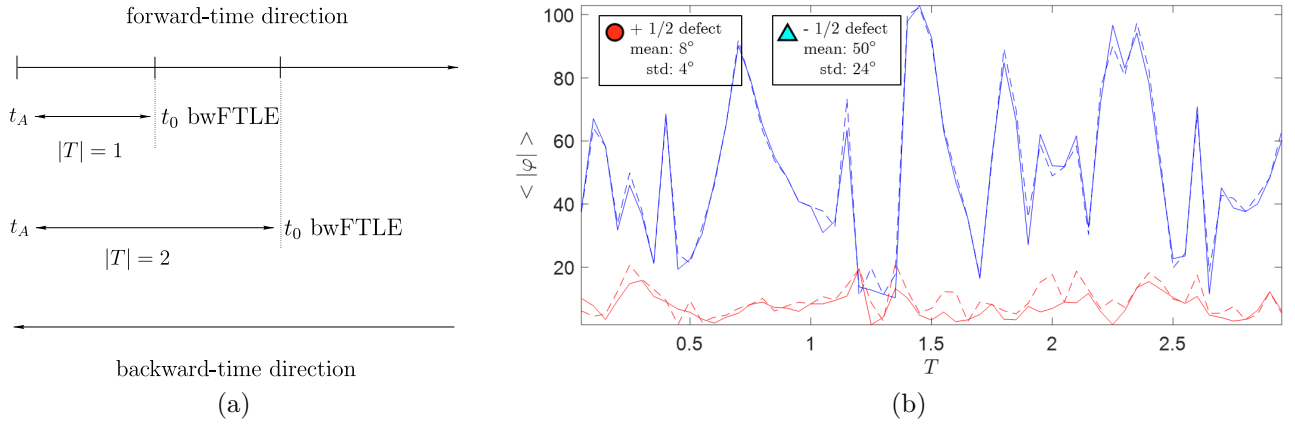


Figure S3: (a) Time intervals for backward-time FTLE computations. (b) Average angle (solid lines), in degrees, between a vector field describing the deformation of the bw FTLE, and disclination velocities as a function of  $|T|$  for simulated extensile active nematics discussed in Fig.4. Dashed lines show the same quantities of solid lines using  $\mathbf{v}$  instead of  $\mathbf{v}_{FTLE}$ . The bw FTLE evolution along with disclination velocities is available as [Movie5](#).

We note that  $T$  automatically specify  $t_0$  and vice-versa because the initial time of our analysis  $t_A$  is fixed. Fig. S3b shows the average angle (solid lines)  $\langle |\varphi| \rangle$  between  $\mathbf{v}_{FTLE}$  and positive and negative disclinations at each  $|T|$ , quantitatively confirming that positive disclinations move in directions similar to  $\mathbf{v}_{FTLE}$  compared to negative disclinations. The overall angular distance between positive disclination and  $\mathbf{v}_{FTLE}$  has a mean of  $8^\circ$ . By contrast, for negative disclinations the average misalignment is  $50^\circ$ . Dashed lines show the same as solid lines using  $\mathbf{v}$  instead of  $\mathbf{v}_{FTLE}$ , highlighting how FTLE evolves almost materially, consistent with [Movie4](#).

Performing the same analysis on the experimental dataset described in Fig. 3, we obtain that the overall angular distance between positive disclination and  $\mathbf{v}_{FTLE}$  has a mean of  $8^\circ$  and a standard deviation of  $4^\circ$ , while  $22^\circ$  and  $15^\circ$  in the case of negative disclinations. [Movie6](#) right panel shows the time evolution of  ${}_b\Lambda$ ,  $\mathbf{v}_{FTLE}$  (green) and  $\mathbf{v}^d$  (red and cyan) along with Lagrangian particles (magenta), confirming quantitatively that positive defects steer and deform  ${}_b\Lambda$ , which in turn organize particles motion. [Movie6](#) left panel shows the director field  $\mathbf{n}$  to confirm the identification of defect type.

## S5 Contractile active nematics

We perform the same analysis described in Fig. 4 in the case of contractile active nematics, simulated using the same parameters of the extensile case and  $\alpha = 25$ . Figure S4 shows the same analysis of Fig. 4. Similarly to the extensile case, disclinations are located in regions of low Lagrangian stretching and high Lagrangian folding (Fig. S4). The  ${}_b\Lambda$  evolution along with disclination velocities is available as [Movie9](#). Performing the same analysis of Fig. S3, we find that the mean angular distance between positive disclination and  $\mathbf{v}_{FTLE}$  has a mean of  $9^\circ$  and a standard deviation of  $6^\circ$ . By contrast, for negative disclinations, the average angular distance has a mean of  $62^\circ$  and a standard deviation of  $32^\circ$ .

Figure S4c shows  ${}_b\Lambda$  for  $|T| = 2$ , along with the position of material particles (magenta) attracted to a  ${}_b\Lambda$  ridge and initially released from a circular blob. Interestingly, Fig. S4c shows

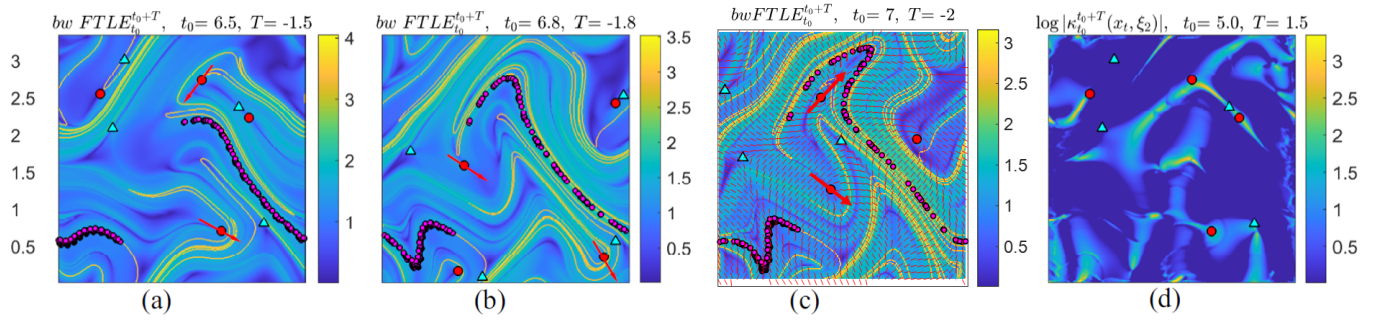


Figure S4: Lagrangian analysis of a simulated contractile active nematic fluid obeying eq. (6). (a)  ${}_b\Lambda$  for  $|T| = 1.5$ , along with the position of material particles (magenta) attracted to a  ${}_b\Lambda$  ridge and initially released from a circular blob. (b-c) Same as (a) for larger  $|T|$ . Red arrows illustrate that  $+1/2$  defects pull the attracting  ${}_b\Lambda$  ridges that, in turn, shape particle motion. In panel c), red lines show the director field. (d) Logarithm of the folding field modulus  $|\kappa_{t_0}^t(\mathbf{x}_t, \xi_2)|$  for  $T = 1.5$  as in (a). [Movie7](#) shows the evolution of panels a,d for different  $T$ . Positive defects are located at regions of high folding-type and low stretching or shearing-type Lagrangian deformation.

that in the case of contractile active nematics,  $\mathbf{n}$  is approximately perpendicular to attractors, as opposed to extensile active nematics (Figs. 3-4 and Fig. S5), in which  $\mathbf{n}$  is approximately parallel to them.

## S6 Analysis of the dancing disclinations flow in confined active nematics

To elucidate the dynamics of the fluctuations of relative angles between  $\mathbf{v}^d$  and  $\mathbf{v}_{FTLE}$  (Fig. S3), we analyze an extensile active nematic fluid confined in a channel<sup>9</sup> in which disclinations undergo a regular motion and the fluid velocity field consists of a vortex lattice (top right panel of [Movie10](#)). In this flow, negative defects oscillate weakly about their average position close to the channel boundaries, while positive defects move along the edge of vortices in the mid-channel region. Similar to the previously analysed flows, the overall angular distance between positive disclination velocities and  $\mathbf{v}_{FTLE}$  has significantly smaller mean and standard deviation compared to those of the negative disclinations (Fig. S5a). Figure S5b shows a snapshot of  ${}_b\Lambda$  for  $|T| = 450$  along with the nematic director field (red) and disclinations. The complete time evolution of panel Fig. S5b is in the top left panel of [Movie10](#). Consistently with Figure 3c, also in this different extensile active nematic fluid,  $\mathbf{n}$  is aligned with attracting  ${}_b\Lambda$  ridges.

As shown in all our examples,  ${}_b\Lambda$  are approximately material, i.e.,  $\mathbf{v}$  is a good approximation of  $\mathbf{v}_{FTLE}$ . Therefore, understanding the alignment of  $\mathbf{v}_{FTLE}$  with the disclination velocities is equivalent to studying the alignment between the fluid velocity at the disclination position and the disclination velocity. The latter, in turn, features two different contributions resulting from the fluid flow and the passive interaction with other defects. That is

$$\mathbf{v}^d = \mathbf{v} - \mu \nabla_{\mathbf{r}} F, \quad (\text{S8})$$

with  $\mu$  a mobility coefficient. As a consequence, an isolated  $+1/2$  disclination moves along the streamlines of the flow, whereas in the presence of other defects this trajectory is perturbed by



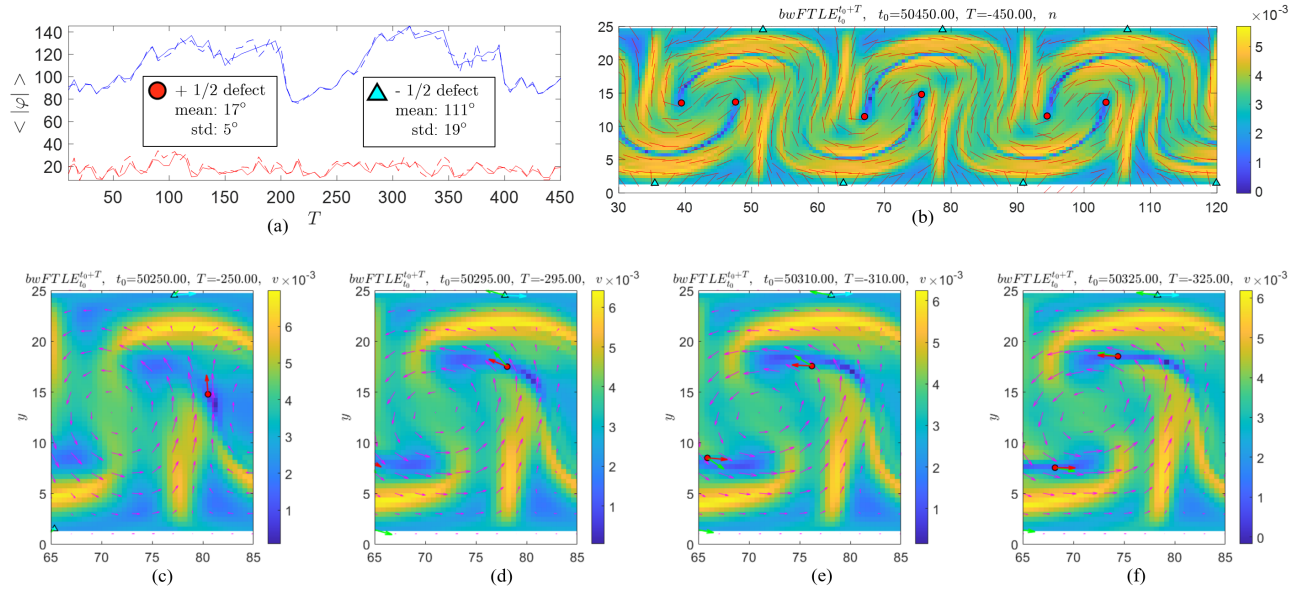


Figure S5: Analysis of the dancing disclination flow<sup>9</sup> representing a simulated extensile active nematic. (a) Same as Fig.S3b. (b)  $b\Lambda$  for  $|T| = 450$  along with the nematic director field (red) and disclinations. The top left panel of [Movie10](#) shows the time evolution of (b) along with the disclination velocities in red and cyan arrows and  $\mathbf{v}_{FTLE}$  (green). The bottom left panel shows the same as the top left panel, with the velocity field (in magenta) instead of  $\mathbf{n}$ . For comparison with typical Eulerian quantities, the bottom right panel shows  $\mathbf{n}$  (red), the leading eigenvector of  $\mathbf{S}$ ,  $\mathbf{e}_2$  (cyan), along with to the leading eigenvector field  $s_2$ . (c-d) Time sequence of a zoomed-in region of the bottom left panel of [Movie10](#), showing  $b\Lambda$ , the motion of disclinations with their velocities (red and cyan), normalized  $\mathbf{v}_{FTLE}$  (green) and  $\mathbf{v}$  (magenta).

the attractive/repulsive forces induced by its neighbors. This dynamics is well exemplified by Figures S5c-d showing a representative zoomed-in region of the bottom left panel of [Movie10](#), in which a positive disclination velocity (red) starts aligned with the fluid velocity (magenta) (c), then deviates from it by crossing instantaneous streamlines (d-e), then realigns with  $\mathbf{v}$ .

These departures from aligned to less aligned disclination and fluid velocities are responsible for the  $\langle |\varphi| \rangle$  oscillations in Fig. S5a, and in the more complex flows we analyzed. A detailed study of what causes these oscillations is outside the scope of this work.

## S7 Relative orientation between $\mathbf{n}$ , $\mathbf{e}_2$ and attracting coherent structures

To shed light on the relative orientation between attractors and the local nematic director, consider the evolution equation for  $\mathbf{Q}$ ,

$$\frac{\overline{D}\mathbf{Q}}{Dt} = \lambda\mathbf{D} + \gamma^{-1}\mathbf{H}, \quad (\text{S9a})$$

$$\mathbf{H} = K\nabla^2\mathbf{Q} + a\mathbf{Q} - b|\mathbf{Q}|^2\mathbf{Q}, \quad (\text{S9b})$$

where  $\frac{\overline{D}\mathbf{Q}}{Dt}$  denotes the co-rotational derivative of  $\mathbf{Q}$ , and  $K, a, b$  are positive constants. In the presence of defects,  $\mathbf{Q}$  is small, therefore the last term in eq. (S9b) is negligible. Neglecting also

the elastic term reorienting the director, we have

$$\frac{\overline{D}\mathbf{Q}}{Dt} \approx \lambda\mathbf{D} + a\gamma^{-1}\mathbf{Q}, \quad (\text{S10})$$

which tends to align  $\mathbf{D}$  with  $-\mathbf{Q}$ . More precisely, the fixed points of this equation satisfy  $\lambda\mathbf{D} = -a\gamma^{-1}\mathbf{Q}$ . We denote by  $\mathbf{e}_1, \mathbf{e}_2$  the eigenvectors of  $\mathbf{D}$  associated with the eigenvalues  $s_1 \leq s_2$ , and note that  $\mathbf{Q}$  has eigenvectors  $\mathbf{n}, \mathbf{n}^\perp$  associated with the eigenvalues  $\alpha S/2, -\alpha S/2$ . Therefore, for extensile active nematics ( $\alpha < 0$ ),  $\lambda\mathbf{D} = a\gamma^{-1}|\alpha|S[\mathbf{n} \otimes \mathbf{n} - \mathbf{I}/2]$ . The leading eigenvector of the tensor on the right-end side is  $\mathbf{n}$ , hence  $\mathbf{e}_2 \parallel \mathbf{n}$ . By contrast, for contractile active nematics ( $\alpha > 0$ ), the leading eigenvector of the tensor on the right-end side is  $\mathbf{n}^\perp$ , leading to  $\mathbf{e}_2 \parallel \mathbf{n}^\perp$ . This argument provides precise connections between  $\mathbf{n}$  and Eulerian (or short-time) attractors and repellers<sup>10</sup>, which are parallel to  $\mathbf{e}_2$  and  $\mathbf{e}_1$ .

To connect  $\mathbf{e}_2$  with Lagrangian attractors, we note that the highest shrinking rate quantified by  ${}_b\Lambda$  is experienced by the material fiber that at the final time is along the leading eigenvector  ${}_b\xi_2$  of the Cauchy-Green tensor computed in backward time (Fig. S6a). Therefore, the attraction is towards  ${}_b\xi_1 \perp {}_b\xi_2$ . At the initial time, the preimage of the  ${}_b\xi_1$  direction is along  ${}_f\xi_2$ , the leading eigenvector of the Cauchy-Green computed in forward time. In<sup>11</sup>, we show analytically that  ${}_f\xi_2$  coincides with  $\mathbf{e}_2$  over short times. More generally, after a finite-time interval, the deformation of a fluid patch depends on the deformation history encoded in the Cauchy-Green tensor and the current stretching rate encoded in  $\mathbf{D}$ . If the latter is aligned with the former, then  $\mathbf{e}_2$  is approximately parallel to  ${}_b\xi_2$  regardless of the short-time assumption used in<sup>11</sup>. This is typically the case in extensile (contractile) active nematics, as the leading stretching direction, and hence the direction of attractors, is approximately parallel (perpendicular) to  $\mathbf{n}$  (Fig. S6a right) because active stresses are dominant<sup>1</sup>. To further support our argument, Fig. S6b-c show that ridges of  ${}_b\Lambda$  are approximately parallel to  ${}_b\xi_1$  (black),  $\mathbf{e}_2$  (white) and  $\mathbf{n}$ , for the extensile experimental data analysed in Fig. 3. In summary, we provided a mechanistic explanation relating the relative orientation between  $\mathbf{n}$ ,  $\mathbf{e}_2$ , and attractors for extensile and contractile active nematic flows, consistent with our numerical and experimental results (Figs.3c,4c, Figs. S4c,S5b).

## S8 Positional coherence as a function of time and activity

We quantify how coherence varies with the time scale  $T$  and the activity parameter  $\alpha$ , by studying the stirring exerted by an incompressible contractile active nematic flow on a passive scalar  $c(\mathbf{x}, t)$ . The passive scalar evolves according to

$$\partial_t c + \mathbf{v} \cdot \nabla c = 0 \quad (\text{S11})$$

with the initial condition  $c(\mathbf{x}, t_0) = c_0(\mathbf{x})$ . To measure stirring, we use the  $H^{-1}$  mixing norm, broadly adopted in fluid flows<sup>13</sup>, and defined as

$$\|c(\cdot, t)\|_{H^{-1}}^2 = \|\nabla^{-1}c(\cdot, t)\|_{L^2}^2 = \sum_{\mathbf{k} \neq 0} |\mathbf{k}|^{-2} |\hat{c}_{\mathbf{k}}(t)|^2, \quad (\text{S12})$$

---

<sup>1</sup>Our argument is consistent with<sup>12</sup>, who first used observations from microtubules images to associate the leading stretching direction with  $\mathbf{n}$  in extensile active nematics.

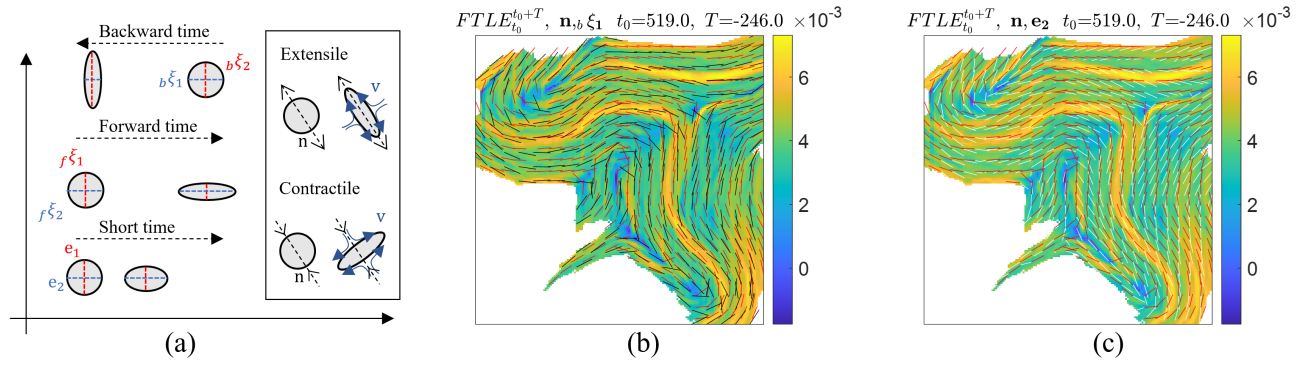


Figure S6: Relative orientation between  $\mathbf{n}$ ,  $\mathbf{e}_2$  and attractors. (a) Left. Deformation of a fluid patch in backward and forward time, and its connection with the forward (backward) Cauchy-Green eigenvectors  $f\xi_1, f\xi_2$  ( $b\xi_1, b\xi_2$ ) and  $\mathbf{D}$  eigenvectors  $\mathbf{e}_1, \mathbf{e}_2$ . Right. Deformation of fluid patch induced by active stresses in extensile and contractile nematics. (b)  ${}_b\Lambda$  for  $|T| = 246$  along with  $\mathbf{n}$  (red) and  $b\xi_1$  (black) for the experimental extensile active nematic analysed in Fig. 3. (c)  ${}_b\Lambda$  for  $|T| = 246$  along with  $\mathbf{n}$  (red) and  $\mathbf{e}_2$  (white) for the extensile active nematics analysed in Fig. 3. [Movie11](#) shows the time evolution of panels b-c.

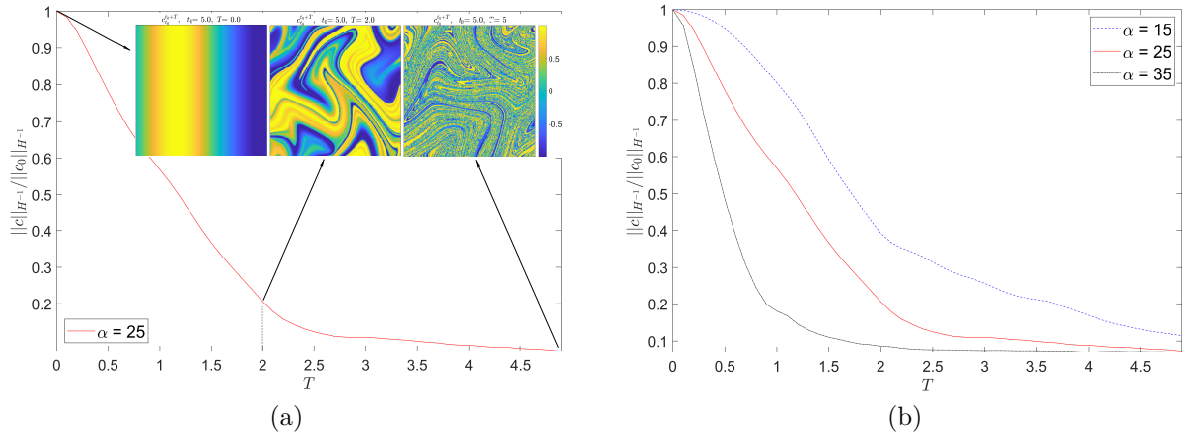


Figure S7: (a)  $H^{-1}$  mixing norm normalized by its initial value for the activity value  $\alpha = 25$ . The insets show the concentration fields at different times computed solving Eq. (S11) with initial distribution  $c_0(\mathbf{x}) = \sin x$ . The complete time evolution of the concentration field is available as [Movie12](#). (b) Same as (a) for different activity values.

where

$$\hat{c}_{\mathbf{k}}(t) = \frac{1}{L} \int_{[0,L]^2} e^{-i\mathbf{k}\cdot\mathbf{x}} c(\mathbf{x}, t) d\mathbf{x} \quad (\text{S13})$$

are the Fourier coefficients of  $c(\mathbf{x}, t)$ . The  $H^{-1}$  measures the variance of a low-pass-filtered image of the concentration field; the smaller it is, the less coherence (more mixed) is the scalar field on large spatial scales. In our analysis,  $c_0(\mathbf{x}) = \sin x$ .

Fig. [S7a](#) shows the  $H^{-1}$  mixing norm normalized by its initial value as a function of  $T$  for nematic flow analyzed in Fig. [S4](#), with activity value  $\alpha = 25$ . The insets show the concentration fields at three different times, while the complete time evolution is available as [Movie12](#). Fig. [S7b](#) shows the normalized  $H^{-1}$  mixing norm for three different values of activity. As expected, spatial coherence decreases with increasing  $T$ , and higher activity  $\alpha$ . We note that the activity values

used here are higher than those seen in typical biological nematic systems such as epithelial, fibroblast and stem cells<sup>14</sup>, where positional coherence is present for larger  $T$ .

## S9 Lagrangian vs Eulerian quantities

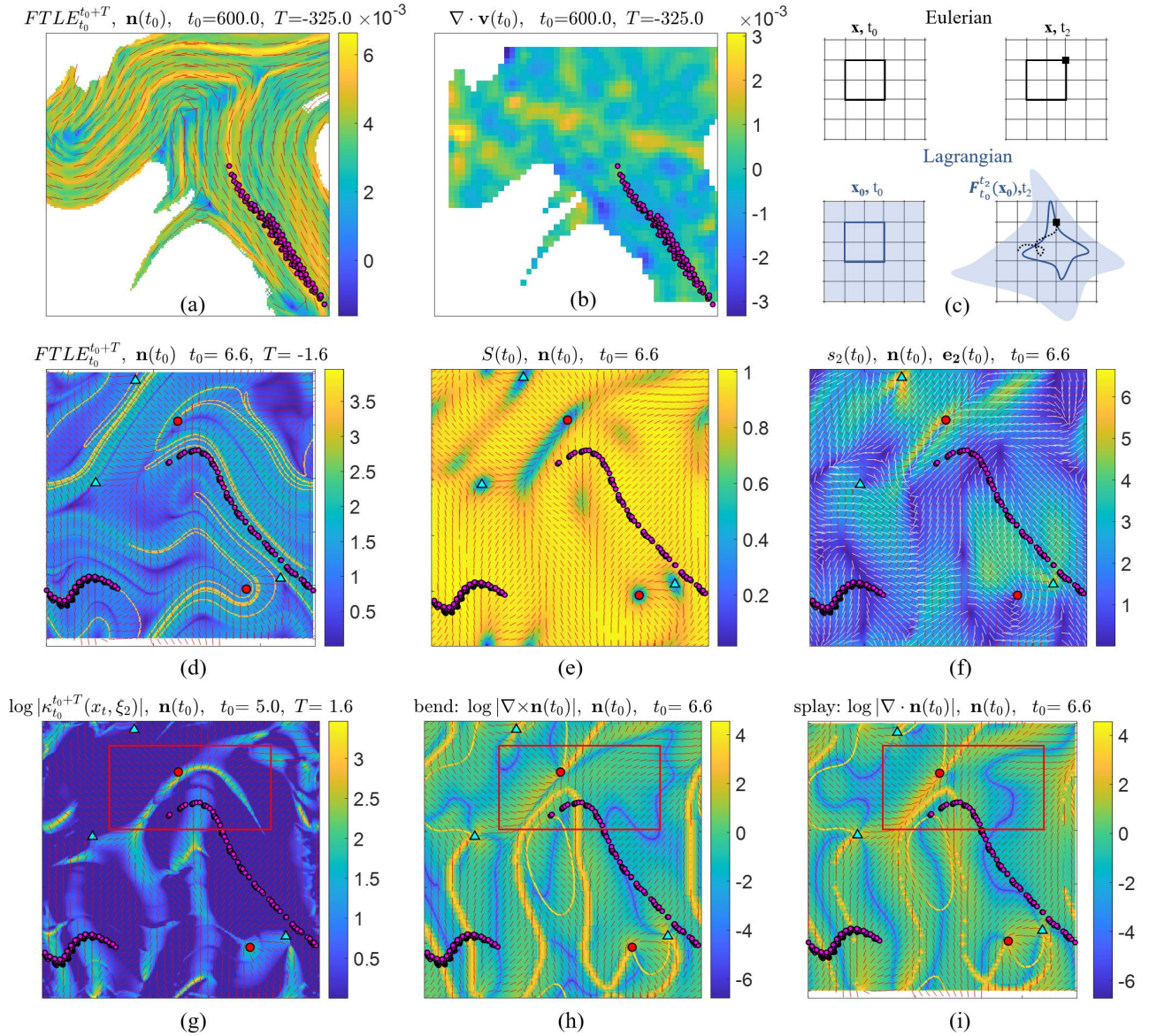
Here we compare Lagrangian fields with the corresponding commonly used Eulerian quantities. Figure S8a shows a time frame of  ${}_b\Lambda$ ,  $\mathbf{n}$  (red) and Lagrangian particles position (magenta) associated with the experimental data described in Fig. 3. Figure S8b shows particles position and  $\nabla \cdot \mathbf{v}$ , a commonly used Eulerian diagnostic to identify regions of particles accumulation<sup>2</sup>. Figure S8b shows that the flow is approximately incompressible ( $\nabla \cdot \mathbf{v} \approx 0$ ) and attractors remain hidden to  $\nabla \cdot \mathbf{v}$ , while being identified by  ${}_b\Lambda$  which captures contributions from both isotropic (due to compressibility) and anisotropic (due to area-preserving) Lagrangian deformations (SI, Section 2c of<sup>16</sup> for a detailed explanation). [Movie13](#) shows the time evolution of panels a-b, as well as the maximum eigenvalue  $s_2$  of the rate of strain tensor and its associated eigenvector  $\mathbf{e}_2$  (white). These results confirm that Lagrangian structures contained in  ${}_b\Lambda$  remain hidden to typical Eulerian quantities as  $\mathbf{n}$ ,  $S$ ,  $\mathbf{e}_2$ ,  $s_2$  and  $\nabla \cdot \mathbf{v}$ .

Figures S8d-i show a time frame of Lagrangian and Eulerian quantities associated with the simulated contractile active nematic described in Fig. S4. Panels d-f show  ${}_b\Lambda$ ,  $\mathbf{n}$ , the nematic order parameter  $S$ ,  $\mathbf{e}_2$ ,  $s_2$  and Lagrangian particles position. As in panels a-b, the attractors captured by  ${}_b\Lambda$  remain hidden to Eulerian fields. Interestingly,  $\mathbf{n}$  can be approximately parallel (a) or perpendicular (d) to  ${}_b\Lambda$  ridges, as explained in SI Sec. 7. In both cases, however, there are no Eulerian quantities able to identify which set of the domain corresponds to an attracting LCS. Panels g-i show the Lagrangian folding map, the Eulerian fields quantifying bend and splay distortions of the director,  $\mathbf{n}$  and particles position. Similar to stretching deformations, Lagrangian folding maps cannot be identified by inspections of Eulerian inhomogeneities of  $\mathbf{n}$  (e.g., the red inset marks regions of high Lagrangian folding and low bend and splay distortions). [Movie14](#) shows the time evolution of panels d-i.

More generally, the nematodynamic PDE (eq. 6) is an Eulerian balance relating  $\mathbf{v}(\mathbf{x}, t)$ ,  $\mathbf{n}(\mathbf{x}, t)$  and their spatial derivatives at any  $\mathbf{x}, t$ . If we consider two times  $t_0$  and  $t_2 = t_0 + T$  and denote by  $\mathbf{F}_{t_0}^{t_2}(\mathbf{x}_0) = \mathbf{x}_0 + \int_{t_0}^{t_2} \mathbf{v}(\mathbf{F}_{t_0}^\tau(\mathbf{x}_0), \tau) d\tau$  the trajectories of particles from  $t_0$  and  $t_2$ , information such as  $\mathbf{F}_{t_0}^{t_2}(\mathbf{x}_0)$  or  ${}_b\Lambda$  are invisible to eq. 6 evaluated from  $t_0$  to  $t_2$  because (eq. 6) does not include  $\mathbf{F}_{t_0}^t(\mathbf{x}_0)$ -dependent terms. Therefore, while a Lagrangian quantity at  $(\mathbf{x}_2, t_2)$  (black square in Fig. S8c) has integrated information along trajectories (dashed black line), these remain hidden to Eulerian quantities at  $(\mathbf{x}_2, t_2)$ .

---

<sup>2</sup>Note that using  $\nabla \cdot \mathbf{v}$  as a diagnostic for attractors can generate both false positives and false negatives, as explained in SFig 2 of<sup>15</sup>.



## S10 Stress at $+1/2$ defects

To quantify the correlation between the total stress and the location and dynamics of topological defects, we consider the solution of the neamtodynamic model (6) analyzed in Fig.S4 and Fig.4. We first note that both the deviatoric viscous stress  $\sigma^v$  and the elastic stress  $\sigma^e = -\lambda S\mathbf{H} + \mathbf{QH} - \mathbf{HQ}$  are traceless; the former follows from incompressibility, while the latter follows because  $\text{tr}[\mathbf{H}] = \partial F_{LdG}/\partial Q_{11} + \partial F_{LdG}/\partial Q_{22} = 0$ ,  $Q_{11} = -Q_{22}$  and  $\text{tr}[\mathbf{QH} - \mathbf{HQ}] = 2\text{tr}[\text{skew}(\mathbf{QH})] = 0$ . Finally, the active stress is also traceless because  $\text{tr}[\sigma^a] = \alpha \text{tr}[\mathbf{Q}] = 0$ . Thus, the maximum and minimum eigenvalues of the above stress tensors have equal magnitude and opposite signs, hence providing a scalar representation of both their maximum and minimum stress contributions.

### Contractile case

Here we analyze the contractile active nematic described in SI Section 5. Figures S9a-d show the maximum eigenvalue of  $\sigma^v, \sigma^e, \sigma^a$  and the total deviatoric stress  $\sigma^D = \sigma^v + \sigma^e + \sigma^a$ , along with the defects location and the nematic director field (red). We find that the maximum total deviatoric stress is minimum at defects (Fig. S9d and Fig. S9g, which shows a zoomed version of the inset in Fig. S9d), meaning that the defect locations are regions subject to minimum shear stress. The black arrows in Fig. S9g represent the leading eigenvector field of  $\sigma^D$ . Because  $\sigma^v, \sigma^e, \sigma^a$  are traceless, the only isotropic stress  $\sigma^I = -p\mathbf{I}$  is given by the pressure. With our convention, positive pressure indicates compressing isotropic stress. Following the numerical scheme in<sup>7</sup>, we have solved eq.(6) by using the streamfunction-vorticity formulation. To recover the pressure, we solve the Poisson equation

$$\nabla^2 p = \nabla \cdot [\nabla \cdot [\sigma^e + \sigma^a]], \quad (\text{S14})$$

obtained by taking the divergence of eq. (6a), and using incompressibility. Solving eq. (S14), we determine the pressure distribution up to a constant that will not affect the pressure topology. Here we set this constant such that the spatial average of the pressure is zero. Figures S9e,h show the pressure field normalized by the maximum pressure in absolute value. Interestingly, we find that positive defects are typically located in regions of low isotropic stress. A closer look at Figs. S9g,h, reveals that while deviatoric and isotropic stresses are low at positive defects, the corresponding stress gradients are high. In Fig. S9l, we show that the topology of both the deviatoric and isotropic stresses induce differential stresses (blue), perpendicular to the  $+1/2$  defect orientation, that bends the active nematic towards the head of the defect. This peculiar stress distribution leaves a clear kinematic footprint in the deformation of the nematic medium, as shown by the high values of Lagrangian folding at  $+1/2$  defects (Fig. S4d), as well as the Eulerian folding rate along  $\mathbf{n}$ , computed from eq. (S3) and shown in Figs. S9f,i.

### Extensile case

Here we analyze the extensile active nematic described in Fig.4. Figure S10 shows the same analysis of Fig. S9 for extensile active nematics, obtained by solving eq.(6) using the same parameters as the contractile case and  $\alpha = -25$ . It is worth pointing out that Fig. S10h is similar to the experimentally measured isotropic stress within monolayers of MDCK (Madin Darby canine kidney) cells, in the vicinity of  $\pm 1/2$  nematic defects in the cell orientation field<sup>17</sup>. Indeed, Fig.3a of<sup>17</sup> shows that  $+1/2$  defects are located in a region of zero isotropic stress,

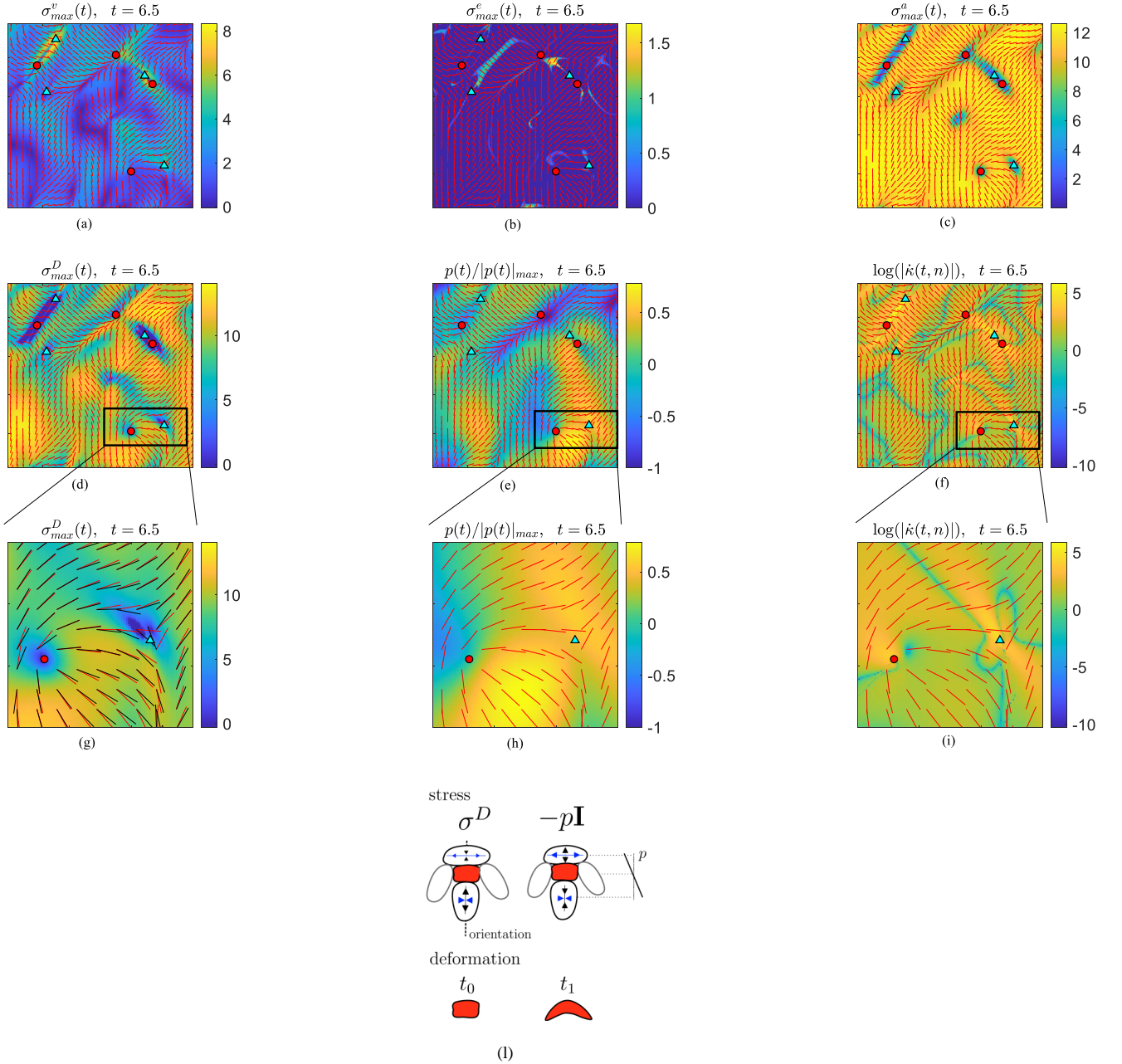


Figure S9: Stress associated with a simulated contractile active nematic ( $\alpha > 0$ ). (a-d) Maximum eigenvalue of  $\sigma^v, \sigma^e, \sigma^a, \sigma^D = \sigma^v + \sigma^e + \sigma^a$ , along with the topological  $+1/2$  (circles),  $-1/2$  (triangles) and the nematic director field in red. (e) Pressure field normalized by the spatial maximum pressure in absolute value completely characterizes the isotropic stress  $\sigma^I = -p\mathbf{I}$ . (f) Logarithm of the folding rate modulus of the active nematic, computed from eq. (S3). (g-i) Zoomed view of the insets in (d-f). The black direction field in (g) shows the leading eigenvector of  $\sigma^D$ . The time evolution of the above panels is available as [Movie15](#). (l) Schematic of the local stress and deformation around a  $+1/2$  defect. Top: Sketch of the deviatoric and isotropic stress distribution (consistent with panels g,h) near a  $+1/2$  defect. The arrow size is proportional to the stress level, and blue marks the direction perpendicular to the defect orientation. Bottom: sketch of the material deformation induced by the stress distribution in neighborhood of a  $+1/2$  defect.

and high isotropic stress gradient along the orientation of the defect, precisely as in Fig. S10h. As in the contractile case, at  $+1/2$  defects the deviatoric stress is zero and has a significant gradient along the defect's orientation (Fig. S10g). Figure S10l shows the effect of the stress distribution around the  $+1/2$  defects, which induces high folding as confirmed both by the Lagrangian finite-time folding (Fig. 4d) and the Eulerian folding rate (Fig. S10i). The peculiar stress distribution of low stress and high stress gradients around  $+1/2$  defects is present in both contractile and extensile active nematics. In the former, the stress gradient induces a folding deformation towards the head of the defect (Fig. S9l), while in the latter towards the tail (Fig. S10l).

The differential stress at negative defects is multiple times smaller compared to the one at positive defects. This can be assessed as follows. An approximate expression for the velocity field in the neighborhood of a defect, can be obtained from solving the Stokes equation with a body force  $\mathbf{f} = \nabla \cdot \boldsymbol{\sigma}^a$ , with  $\boldsymbol{\sigma}^a$  the active stress associated to a defective configuration of the nematic director, i.e.  $\mathbf{n}_{\pm} = \cos(\phi/2) \mathbf{e}_x \pm \sin(\phi/2) \mathbf{e}_y$  (see e.g.<sup>18</sup>). This gives the following velocity

$$\mathbf{v}_+ = \frac{\alpha}{12\eta} \{ [3(R-r) + r \cos 2\phi] \mathbf{e}_x + r \sin 2\phi \mathbf{e}_y \} ,$$

$$\mathbf{v}_- = \frac{\alpha r}{12\eta R} \left\{ \left[ \left( \frac{3}{4} r - R \right) \cos 2\phi - \frac{R}{5} \cos 4\phi \right] \mathbf{e}_x - \left[ \left( \frac{3}{4} r - R \right) \sin 2\phi + \frac{R}{5} \sin 4\phi \right] \mathbf{e}_y \right\} ,$$

and pressure fields

$$p_+ = p_0 + \frac{\alpha}{2} \cos \phi , \quad p_- = p_0 - \frac{\alpha}{6} \cos 3\phi ,$$

with  $R$  a length scale representing the size of the neighborhood. Because  $\pm 1/2$  defects are in fact minimizers of the Frank free energy  $F = K/2 \int dA |\nabla \mathbf{n}|^2$ , the elastic stress associated with this solution is identically zero (in experiments, where the configuration of the director is not that of an ideal defect, the elastic stress does not vanish, but is nevertheless expected to be small compared to other contributions), thus

$$\boldsymbol{\sigma} = -p\mathbf{I} + \eta [\nabla \mathbf{v} + (\nabla \mathbf{v})^T] + \alpha \left( \mathbf{n} \otimes \mathbf{n} - \frac{1}{2} \mathbf{I} \right) .$$

Replacing the previous expressions of  $\mathbf{n}_{\pm}$ ,  $\mathbf{v}_{\pm}$  and  $P_{\pm}$  into this, one finds that  $\sigma_{xy} = 0$ , thus the total of the stress is solely given by the aforementioned pressure field. Next, computing  $P_{\pm}$  at  $y = 0$  – that is, along the longitudinal direction of  $+1/2$  defects and along one of the three equivalent longitudinal directions for  $-1/2$  defects – readily yields

$$p_+(x, 0) = p_0 + \frac{\alpha}{2} \text{sign}(x) , \quad p_-(x, 0) = p_0 - \frac{\alpha}{6} \text{sign}(x) .$$

The stress difference across defects is then

$$\Delta p_+ = \alpha \quad \Delta p_- = -\frac{\alpha}{3} ,$$

as anticipated. In experiments, when the director  $\mathbf{n}$  departs from the ideal defective configuration  $\mathbf{n}_{\pm}$ , this discontinuous pressure profile is expected to be replaced by a smooth and yet sharp pressure gradient and milder anisotropic stresses, but without substantially changing this picture.



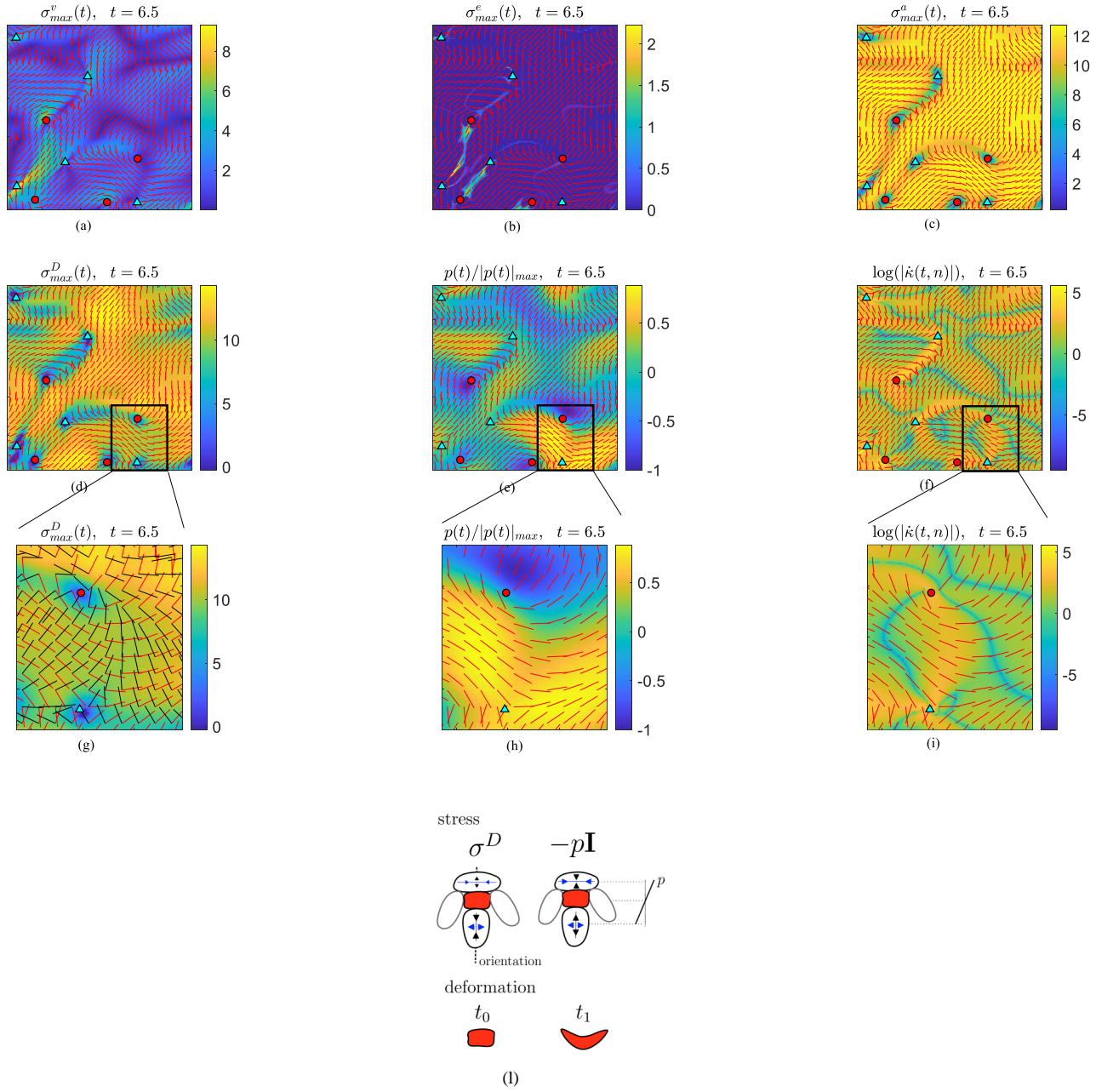


Figure S10: Stresses associated with a simulated extensile active nematic ( $\alpha = -25$ ) following the analysis shown in Fig. S9. The time evolution of the above panels is available as [Movie16](#). Compare panel h with with Fig. 3a in<sup>17</sup>, which shows the experimentally measured isotropic stress within monolayers of MDCK (Madin Darby canine kidney) cells, in the vicinity of  $\pm 1/2$  nematic defects in the cell orientation field.

## References

- [1] M. Serra, J. Vétel, and G. Haller, “Exact theory of material spike formation in flow separation,” *J. Fluid Mech.*, vol. 845, pp. 51–92, 2018.
- [2] S. DeCamp, G. Redner, A. Baskaran, M. Hagan, and Z. Dogic, “Orientational order of motile defects in active nematics,” *Nature materials*, vol. 14, no. 11, p. 1110, 2015.
- [3] L. M. Lemma, S. J. DeCamp, Z. You, L. Giomi, and Z. Dogic, “Statistical properties of autonomous flows in 2d active nematics,” *Soft Matter*, vol. 15, pp. 3264–3272, 2019.
- [4] M. Shribak and R. Oldenbourg, “Techniques for fast and sensitive measurements of two-dimensional birefringence distributions,” *Appl. Opt.*, vol. 42, no. 16, pp. 3009–3017, 2003.
- [5] A. M. Tayar, L. M. Lemma, and Z. Dogic, “Assembling microtubule-based active matter,” in *Microtubules*, pp. 151–183, Springer, 2022.
- [6] M. Kleman and O. D. Lavrentovich, *Soft matter physics: an introduction*. Springer, 2003.
- [7] L. Giomi, “Geometry and topology of turbulence in active nematics,” *Phys. Rev. X*, vol. 5, no. 3, p. 031003, 2015.
- [8] X. Tricoche and G. Scheuermann, “Topology simplification of symmetric, second-order 2d tensor fields,” in *Geometric Modeling for Scientific Visualization*, pp. 275–291, Springer, 2004.
- [9] T. N. Shendruk, A. Doostmohammadi, K. Thijssen, and J. M. Yeomans, “Dancing disclinations in confined active nematics,” *Soft Matter*, vol. 13, no. 21, pp. 3853–3862, 2017.
- [10] M. Serra and G. Haller, “Objective Eulerian coherent structures,” *Chaos*, vol. 26, no. 5, p. 053110, 2016.
- [11] P. J. Nolan, M. Serra, and S. D. Ross, “Finite-time lyapunov exponents in the instantaneous limit and material transport,” *Nonlinear Dynamics*, vol. 100, no. 4, pp. 3825–3852, 2020.
- [12] A. J. Tan, E. Roberts, S. A. Smith, U. A. Olvera, J. Arteaga, S. Fortini, K. A. Mitchell, and L. S. Hirst, “Topological chaos in active nematics,” *Nature Physics*, vol. 15, no. 10, pp. 1033–1039, 2019.
- [13] C. R. Doering and J.-L. Thiffeault, “Multiscale mixing efficiencies for steady sources,” *Physical Review E*, vol. 74, no. 2, p. 025301, 2006.
- [14] A. Doostmohammadi, J. Ignés-Mullol, J. Yeomans, and F. Sagués, “Active nematics,” *Nature communications*, vol. 9, no. 1, p. 3246, 2018.
- [15] M. Serra, P. Sathe, I. Rypina, A. Kirincich, S. D. Ross, P. Lermusiaux, A. Allen, T. Peacock, and G. Haller, “Search and rescue at sea aided by hidden flow structures,” *Nature Communications*, vol. 11, no. 1, pp. 1–7, 2020.

- [16] M. Serra, S. Streichan, M. Chuai, C. J. Weijer, and L. Mahadevan, “Dynamic morphoskeletons in development,” *Proceedings of the National Academy of Sciences*, vol. 117, no. 21, pp. 11444–11449, 2020.
- [17] T. Saw, A. Doostmohammadi, V. Nier, L. Kocgozlu, S. Thampi, Y. Toyama, P. Marcq, C. Lim, J. Yeomans, and B. Ladoux, “Topological defects in epithelia govern cell death and extrusion,” *Nature*, vol. 544, no. 7649, p. 212, 2017.
- [18] L. A. Hoffmann, K. Schakenraad, R. M. Merks, and L. Giomi, “Chiral stresses in nematic cell monolayers,” *Soft matter*, vol. 16, no. 3, pp. 764–774, 2020.